



OPEN

## Hydrological projections in the upper reaches of the Yangtze River Basin from 2020 to 2050

Ya Huang<sup>1,2,3,4✉</sup>, Weihua Xiao<sup>1</sup>, Baodeng Hou<sup>1</sup>, Yuyan Zhou<sup>1</sup>, Guibing Hou<sup>3</sup>, Ling Yi<sup>3</sup> & Hao Cui<sup>1</sup>

Understanding the impact of climate change on runoff is essential for effective water resource management and planning. In this study, the regional climate model (RCM) RegCM4.5 was used to dynamically downscale near-future climate projections from two global climate models to a 50-km horizontal resolution over the upper reaches of the Yangtze River (UYRB). Based on the bias-corrected climate projection results, the impacts of climate change on mid-twenty-first century precipitation and temperature in the UYRB were assessed. Then, through the coupling of a large-scale hydrological model with RegCM4.5, the impacts of climate change on river flows at the outlets of the UYRB were assessed. According to the projections, the eastern UYRB will tend to be warm-dry in the near-future relative to the reference period, whereas the western UYRB will tend to be warm-humid. Precipitation will decrease at a rate of 19.05–19.25 mm/10 a, and the multiyear average annual precipitation will vary between – 0.5 and 0.5 mm/day. Temperature is projected to increase significantly at a rate of 0.38–0.52 °C/10 a, and the projected multiyear average air temperature increase is approximately 1.3–1.5 °C. The contribution of snowmelt runoff to the annual runoff in the UYRB is only approximately 4%, whereas that to the spring runoff is approximately 9.2%. Affected by climate warming, the annual average snowmelt runoff in the basin will be reduced by 36–39%, whereas the total annual runoff will be reduced by 4.1–5%, and the extreme runoff will be slightly reduced. Areas of projected decreased runoff depth are mainly concentrated in the southeast region of the basin. The decrease in precipitation is driving this decrease in the southeast, whereas the decreased runoff depth in the northwest is mainly driven by the increase in evaporation.

In the past few decades, the significant increase in temperature has led to an increase in the maximum amount of water vapor that can be carried by the atmosphere, which has affected the spatial and temporal distribution characteristics of precipitation<sup>1–5</sup>. Higher temperature also causes higher rates of surface drying and evaporation, thereby increasing the duration and intensity of droughts<sup>6</sup>. Many regions of the world can easily cope with moderate changes in the average climate and can even benefit from changing climate<sup>7</sup>. However, most of the destructive effects of floods, droughts or other disasters are the result of extreme weather and climate events, which are likely to occur more frequently on a global scale<sup>8</sup> and have indirect and direct impacts on natural vegetation, urban construction, farming, energy generation, water resources and the environment<sup>9–12</sup>, resulting in considerable economic losses<sup>13</sup>. Accurate understanding and projections of the spatiotemporal characteristics of water resource changes in a basin caused by changes in precipitation are essential for effectively managing regional water resources, responding to various risks related to climate change, and formulating appropriate climate change adaptation and mitigation measures<sup>14</sup>.

The Yangtze River, the longest river in China, provides precious water resources for the Yangtze River Basin (YRB) and supports the livelihoods of millions of people. Due to the influences of the East Asian summer monsoon and the South Asian summer monsoon, the YRB exhibits complex and unique precipitation patterns and a unique regional climate<sup>15,16</sup>, and is a flood-prone area<sup>17</sup>. The upper reaches of the YRB (UYRB) accounts for approximately 59% of the YRB, and the multiyear average annual runoff accounts for approximately 46% of the YRB. Climate change has led to changes in the hydrological conditions in the UYRB, which have affected

<sup>1</sup>State Key Laboratory of Simulation and Regulation of Water Cycle in River Catchment, China Institute of Water Resources and Hydropower Research, Beijing 100038, China. <sup>2</sup>College of Oceanography, Hohai University, Nanjing 210098, China. <sup>3</sup>China Water Resources Pearl River Planning, Surveying & Designing Co., Ltd., Zhanyi Road 19#, Guangzhou 510610, China. <sup>4</sup>Global Institute for Water Security, University of Saskatchewan, Saskatoon, SK, Canada. ✉email: hygccw@163.com

the amount of available water resources and the socioeconomic development and ecological environment of the middle and lower reaches of the YRB. For this reason, the impact of climate change on water resources in the UYRB and the future response of water resources in the basin to climate change have received widespread attention. A large number of observations and projection studies suggest that climate change has accelerated the hydrological cycle of the YRB, reduced the snow cover in the basin and increased extreme runoff. Previous studies have mainly used climate conditions predicted by global climate models (GCMs) to drive hydrological models to study the responses of UYRB hydrology to climate change<sup>18–26</sup>. However, few studies have investigated the hydrological changes in the UYRB under climate change using a coupling model based on the RegCM4 and variable infiltration capacity (VIC) models<sup>27–29</sup>.

RegCM has been applied to the UYRB as an effective tool for assessing and projecting hydroclimatic conditions<sup>27–31</sup>, but it remains challenging to accurately assess and project climate changes in the basin. Gao et al.<sup>31</sup> found that, according to a coupling model of RegCM2 and CSIRO R21L9, precipitation in most regions of the YRB will increase in the future. Cao et al.<sup>30</sup> found that, based on RegCM3 forcing by the FvGCM CCM3 under the SRES A2 scenario, summer precipitation in most areas of the YRB will decrease by the late twenty-first century. Gu et al.<sup>29</sup> used the ECHAM5 results under the SRES A1B scenario to drive RegCM4 to project precipitation in the YRB to the end of the twenty-first century and found that precipitation in the north and south of the basin will increase and decrease, respectively. Lu et al.<sup>28</sup> used the HadGEM2-ES under three representative concentration pathways (RCPs) scenarios (2.6, 4.5, and 8.5) to drive RegCM4 to project runoff in the source region of YRB for 2041–2060 and found that snowmelt runoff would become more important with increase of 17.5% and 18.3%, respectively, under RCP2.6 and RCP4.5 but decrease of 15.0% under RCP8.5. In general, the above results indicate that the total precipitation and probability of heavy precipitation in the YRB will significantly increase by the end of this century. However, investigations of near-future responses of hydroclimatic processes of the UYRB to global climate change are very limited.

The purpose of the current study was to evaluate the characteristics of changes in runoff in the UYRB under near-future climate change. To this end, the historical and future projection results provided by CSIRO-MK3.6.0 and MPI-ESM-MR were used to conduct a 50-km resolution dynamic downscaling experiment to estimate the characteristics of temperature and precipitation change in the UYRB under two RCPs (4.5 and 8.5) in the mid-twenty-first century. In addition, the quantile mapping method based on the mixed distribution was used to correct the bias of meteorological elements from the dynamic downscaling output of the regional climate model (RCM). Before using the VIC model, the generalized likelihood uncertainty estimation (GLUE) method was used to measure the uncertainty of the parameters of the VIC model. The corrected meteorological elements were used to drive the VIC hydrological model to analyze the impacts of near-future climate change on runoff in the UYRB. This study has certain reference significance for deepening the understanding of runoff change characteristics and water resource management in the UYRB under the background of global warming and provides a scientific basis for further development of adaptive measures.

## Models and data

**The climate model.** *Experimental design and model configuration.* RegCM4.5 is an RCM developed by the Abdus Salam International Center for Theoretical Physics<sup>32</sup> and has been extensively applied in multi-decadal climate change simulations in China<sup>33,34</sup>. Because the RegCM4.5 scheme configured by Gao et al.<sup>33</sup> exhibits good simulation performance in China, it was adopted in this study. As shown in Fig. 1a, in this study, only the UYRB from East Asia was intercepted for analysis<sup>35</sup>. The topography and river system in the UYRB were shown in Fig. 1b. The radiation scheme used was the NCAR CCM3 scheme<sup>36</sup>. The cumulus convection scheme and planetary boundary layer scheme used in the current study were the Emanuel<sup>37</sup> and Holtslag<sup>38</sup> schemes, respectively. The Zeng sea surface flux parameterization scheme was used<sup>39</sup>. Details on the model parameter configuration are presented in Table 1. The processing of and analysis procedures for the various data sets used in this study are shown in Fig. 2.

*Correction of the RegCM4.5 outputs.* The commonly used RCM bias correction methods are the Delta method<sup>40</sup>, statistical multiple regression models<sup>41,42</sup>, K-nearest neighbor approach<sup>43</sup>, nearest-neighbor technique<sup>44</sup>, and quantile mapping<sup>45–47</sup>. Themeßl et al.<sup>47</sup> compared the correction performance of the above methods on RCM output results and found that the quantile mapping (QM) method had the best performance. Moreover, Shin et al.<sup>45</sup> found that the QM method based on the mixed distribution is better than the QM method based on the single distribution in correcting precipitation, especially extreme precipitation. Therefore, the QM method based on the mixture distribution was used to correct the precipitation, and the temperature was corrected by the QM method based on the GEV distribution<sup>48</sup>. Due to the obvious seasonal characteristics of the climate in the YRB, the RCM output was corrected month by month based on long-term observation data.

Some distributions that are widely applied for modeling extreme events in hydrometeorological and many other fields<sup>45,49–51</sup>, such as the gamma, exponential, generalized extreme value (GEV), Gumbel and generalized Pareto (GP) distributions were tested to evaluate the optimal fitting distribution of precipitation events in the UYRB. The cumulative distribution function (CDF) and probability density function (PDF) of the above distributions are shown in Table 2.

The definition of a mixture distribution is as follows:

$$f(x) = \sum_{i=1}^n \sigma_i f_i(x; \delta_i) \quad (1)$$

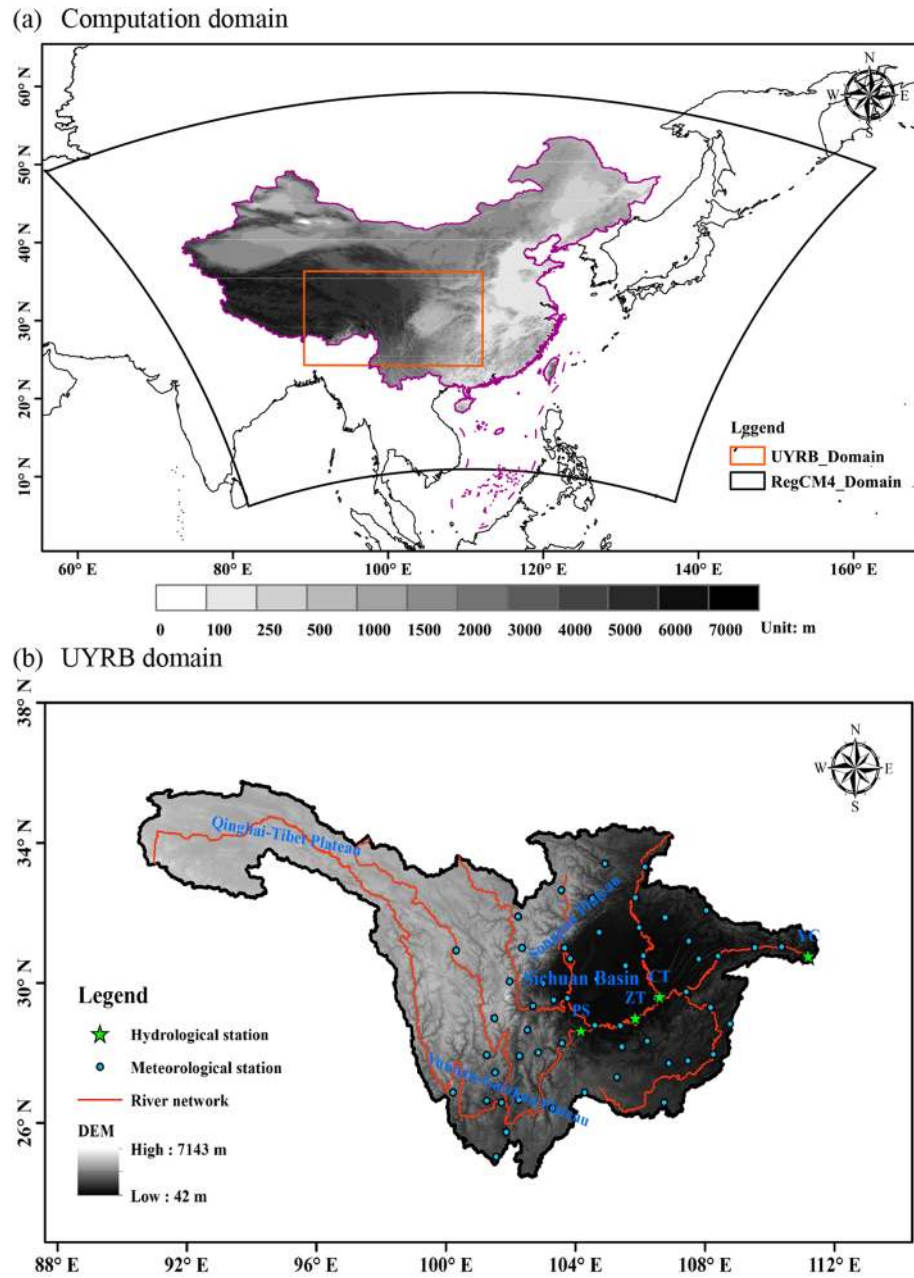


**Figure 1.** (a) Computation domain and topography (m) of RegCM4; (b) the UYRB domain and topography (m). The figure was generated by Arcmap 10.6 (<https://www.esri.com>).

where  $\delta_i$  is a parameter of the  $i$ th distributed component in the mixture distribution, and  $\sigma_i$  is the weight of the  $i$ th distributed component.  $n$  is the number of mixtures applied. Based on the characteristics of the above five distributions, we present five mixture distributions: gamma-gamma (G-G), gamma-exponential (G-E), gamma-Gumbel (G-U), gamma-GEV (G-V) and gamma-GP (G-P). Their PDFs are as follows:

$$f_{G-G}(x; \alpha_1, \beta_1, \alpha_2, \beta_2) = \sigma f_G(x; \alpha_1, \beta_1) + (1 - \sigma) f_G(x; \alpha_2, \beta_2) \tag{2}$$

$$f_{G-E}(x; \alpha_1, \beta_1, \alpha_2) = \sigma f_G(x; \alpha_1, \beta_1) + (1 - \sigma) f_E(x; \alpha_2) \tag{3}$$

$$f_{G-V}(x; \alpha_1, \beta_1, \alpha_2, \beta_2, \gamma) = \sigma f_G(x; \alpha_1, \beta_1) + (1 - \sigma) f_V(x; \alpha_2, \beta_2, \gamma) \tag{4}$$

$$f_{G-U}(x; \alpha_1, \beta_1, \alpha_2, \beta_2) = \sigma f_G(x; \alpha_1, \beta_1) + (1 - \sigma) f_U(x; \alpha_2, \beta_2) \tag{5}$$

Contents	Description
Domain	50 km horizontal resolution Central Lat. and Lon.: 35°N, 115°E 200 (Lon) × 130 (Lat)
Vertical layers (top)	18 vertical sigma levels (1 hPa)
PBL scheme	Holtslag
Cumulus parameterization scheme	Emanuel
Land surface model	NCAR CLM3.5
Short-/longwave radiation scheme	NCAR CCM3
Boundary data	CSIRO-MK3.6.0, MPI-ESM-MR
Simulation period	Jan. 1970-Dec. 2000; Jan. 2020-Dec. 2050
Analysis period	Jan. 1971-Dec. 2000; Jan. 2021-Dec. 2050

**Table 1.** The RegCM4 model configuration used in this study.

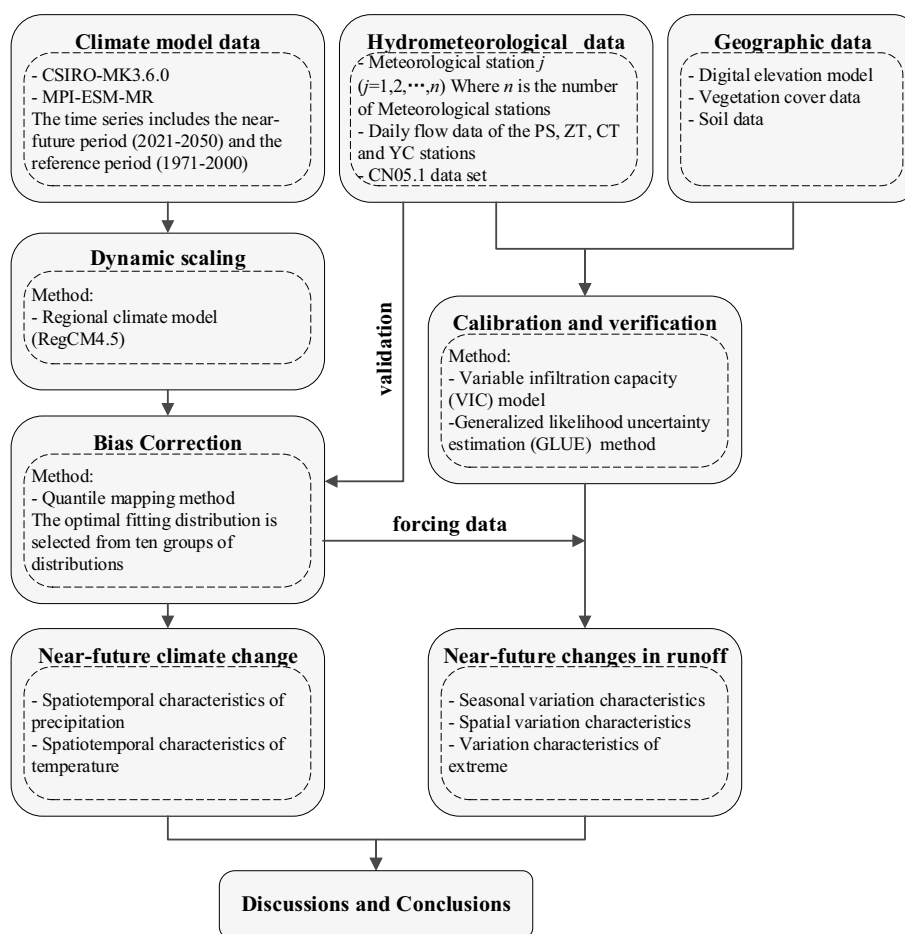


**Figure 2.** Modelling flowchart of this study. The figure was generated by Visio 2019 (<https://www.microsoft.com/>).

$$f_{G-P}(x; \alpha_1, \beta_1, \alpha_2, \beta_2, \gamma) = \sigma f_G(x; \alpha_1, \beta_1) + (1 - \sigma) f_P(x; \alpha_2, \beta_2, \gamma) \quad (6)$$

The simulated precipitation of the RCM usually produces a large number of invalid precipitation events. To be consistent with the observed precipitation events, we corrected the RCM precipitation events based on the historical period.

The simulated precipitation of the RCM usually generates a large number of invalid precipitation events. To be consistent with the observed precipitation events, we corrected the daily RCM precipitation data based on daily precipitation observation data of the reference period. The probability  $P$  that the observation of daily precipitation is zero is defined as follows:

Function	PDF	CDF
Gamma	$f_G(x) = \frac{\alpha^{-\beta}}{\Gamma(\beta)} x^{\beta-1} \exp(-\frac{x}{\alpha})$	$F_G(x) = \int_0^x \frac{\alpha^{-\beta}}{\Gamma(\beta)} x^{\beta-1} \exp(-\frac{x}{\alpha}) dx$
Exponential	$f_E(x) = \frac{1}{\alpha} \exp(-\frac{x}{\alpha})$	$F_E(x) = 1 - \exp(-\frac{x}{\alpha})$
GEV	$f_V(x) = \frac{1}{\alpha} (1 + \beta(-\frac{x-\tau}{\alpha})^{-1/\beta-1}) \exp(-(1 + \beta(\frac{x-\tau}{\alpha})^{-1/\beta}))$	$F_V(x) = \exp(-(1 + \beta(\frac{x-\tau}{\alpha})^{-1/\beta}))$
Gumbel	$f_U(x) = \frac{1}{\alpha} \exp(-\frac{x-\tau}{\alpha}) \exp(-\exp(-\frac{x-\tau}{\alpha}))$	$F_U(x) = 1 - \exp(-\exp(-\frac{x-\tau}{\alpha}))$
GP	$f_P(x) = \frac{1}{\alpha} (1 + \beta(\frac{x-\tau}{\alpha})^{-1/\beta-1})$	$F_P(x) = 1 - (1 + \beta(\frac{x-\tau}{\alpha})^{-1/\beta})$

**Table 2.** PDF and CDF of the functions used in the study.

$$P_0^{obs} = \frac{n_0^{obs}}{N^{obs}} \tag{7}$$

where  $N^{obs}$  is the total number of days during years and  $n_0^{obs}$  is the number of dry days in  $N^{obs}$ . The zero part of the daily precipitation of the outputs is generally smaller than the portion of the observation, i.e.,  $P_0^{RCM} < P_0^{obs}$  for the reference period. Therefore, it is necessary to set the RegCM4.5 precipitation values to zero so that  $P_0^{RCM} = P_0^{obs}$ .

$$x = \begin{cases} x_{RCM} & x_{RCM} > \phi \\ 0 & x_{RCM} \leq \phi \end{cases} \tag{8}$$

where  $\phi$  is the threshold corresponding to RCM when  $P_0^{RCM} = P_0^{obs}$ .

To rapidly obtain the parameters of the mixture distributions, a genetic algorithm was used to optimize the parameters. Three indices, the relative error (*BIAS*), correlation coefficient (*CORR*) and Nash–Sutcliffe efficiency coefficient (*NSE*), were selected as the genetic algorithm optimization objective functions, and the same calculation weight was applied. The formulas of the three indices are as follows:

$$BIAS = \frac{\bar{P} - \bar{O}}{\bar{O}} \times 100\% \tag{9}$$

$$CORR = \frac{\sum_{i=1}^N (P_i - \bar{P})(O_i - \bar{O})}{\left[ \sum_{i=1}^N (P_i - \bar{P})^{0.5} \right] \left[ \sum_{i=1}^N (O_i - \bar{O})^{0.5} \right]} \tag{10}$$

$$NSE = 1 - \frac{\sum_{i=1}^N (P_i - O_i)^2}{\sum_{i=1}^N (O_i - \bar{O})^2} \tag{11}$$

where  $P_i$  and  $O_i$  are the values of the  $i$ -th period in the fitting and observation, respectively;  $\bar{P}$  and  $\bar{O}$  are the average values of the fitting and observation, respectively; and  $N$  is the total number of samples.

**The large-scale hydrological model.** The VIC hydrological model can be used to simultaneously simulate the energy balance and the water balance of the ground surface<sup>52,53</sup>. The model has been widely used in global and regional streamflow studies<sup>54–59</sup>.

*Uncertainty of the VIC model.* In the study, the GLUE method proposed by Beven et al.<sup>60</sup> was used to measure the uncertainty of the parameters of the VIC model. The likelihood objective function (LOF) is mainly used to evaluate the fit between the observed and simulated results. The *NSE* and *BIAS*, two indices with the same weight, were taken into consideration. The LOF is defined as follows:

$$OBJ = 0.5|BIAS| + 0.5(1 - NSE) \tag{12}$$

To obtain the uncertainty range of the VIC hydrological model at a certain confidence level, the LOF values of all parameter groups less than 0.5 were normalized and sorted. To quantify the uncertainty level of the VIC hydrological model, three commonly used evaluation indices were selected for uncertainty analysis. These indices are defined as follows<sup>61</sup>:

$$\text{Containing ratio: } (CR)CR = \frac{n_{Q_m}}{n} \times 100\% \tag{13}$$

where  $n$  is the total number of observed discharges and  $n_{Q_m}$  is the number of observed discharges falling within the uncertainty intervals.

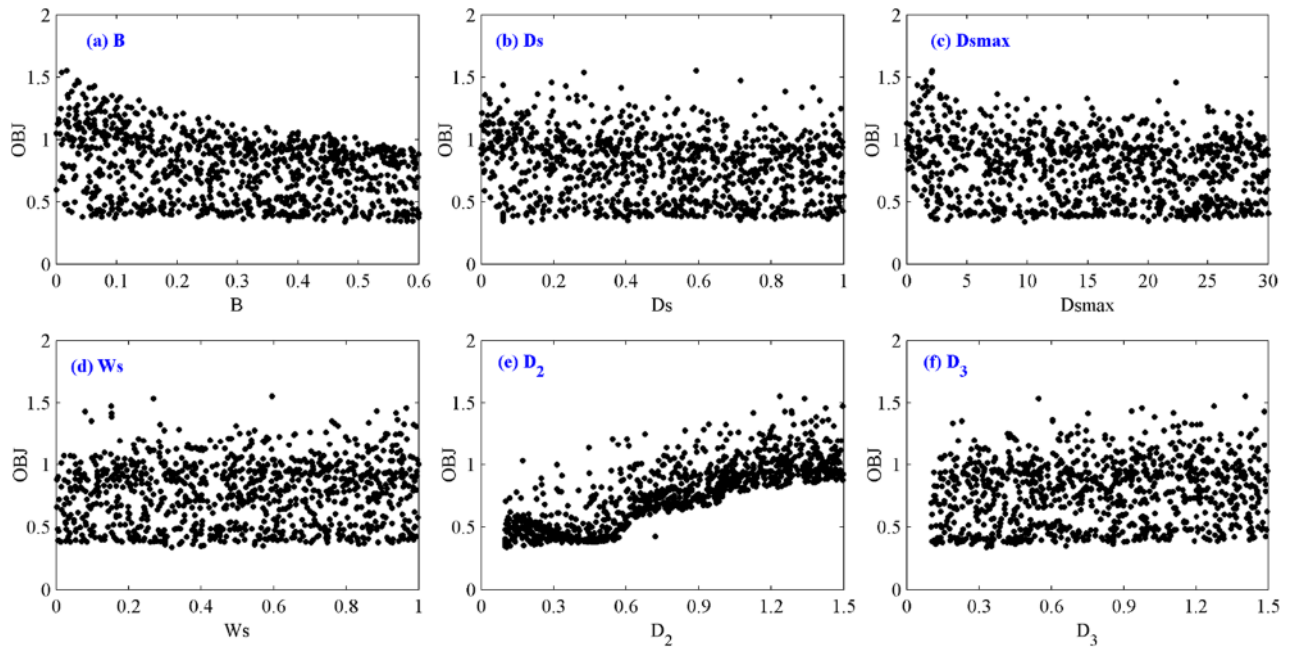


**Figure 3.** Scatter plots of likelihood objective function values for each parameter. The figure was generated by MATLAB2019a (<https://www.mathworks.com/>).

$$\text{Average bandwidth (B)} : B = \frac{1}{n} \sum_{i=1}^n (Q_i^{upper} - Q_i^{lower}) \tag{14}$$

where  $Q_i^{upper}$  and  $Q_i^{lower}$  are the upper and lower values, respectively, at time  $i$ .

$$\text{Average asymmetry degree (S)} : S = \frac{1}{n} \sum_{i=1}^n \left| \frac{Q_i^{upper} - Q_i}{Q_i^{upper} - Q_i^{lower}} - 0.5 \right| \tag{15}$$

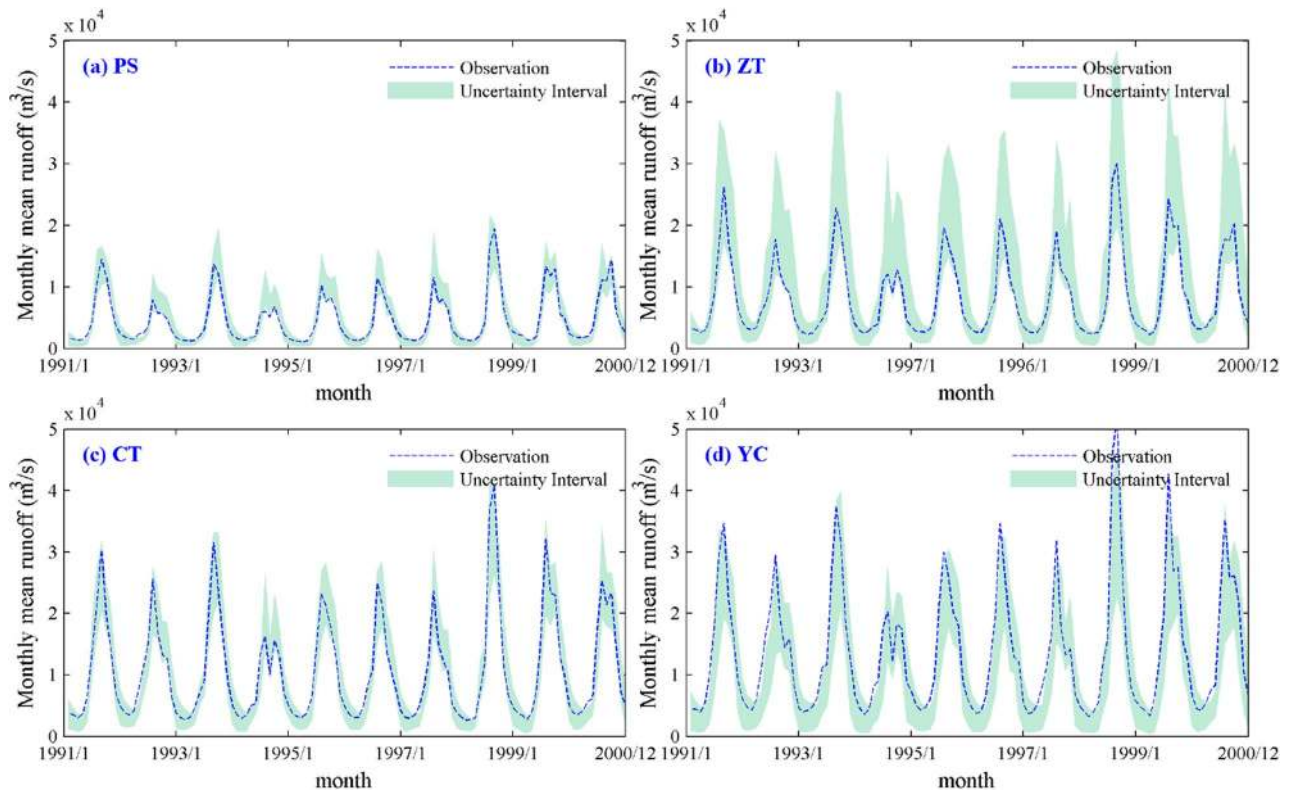
where  $Q_i$  is the observed discharge corresponding to time  $i$ .

Figure 3 shows the scatter plots of the LOF for all parameters after the weighted calculation of four hydrological stations. In Fig. 3b–d, f, the scatter points of the LOF for the  $D_s$ ,  $D_{smax}$ ,  $W_s$  and  $D_3$  are approximately uniformly distributed and exhibit no obvious trend, indicating that these parameters are insensitive. For parameters  $D_2$  and  $B$ , the scatter points are unevenly distributed, which means that  $D_2$  and  $B$  are sensitive. The LOF decreases as  $D_2$  increases from 0.1 to 0.6 and increases as  $D_2$  increases from 0.6 to 1.5 (Fig. 3e). Parameter  $B$  ranges from 0 to 0.6, and the LOF decreases as  $B$  increases (Fig. 3a).

As shown in Fig. 4a–d, the 95% confidence interval covers the observed flow of each station during the verification period, and only a few observed runoffs are outside the confidence interval, indicating that the VIC model is feasible for simulating runoff in the UYRB. The CR values at the Pingshan (PS), Zhutuo (ZT), Cuntan (CT) and Yichang (YC) stations are 77.5%, 98.3%, 79.2% and 75.3%, respectively. The  $B$  values are 3175, 10,736, 6201 and 9732, and the  $S$  values are 0.31, 0.25, 0.29 and 0.35, respectively (Table 3). In general, the VIC hydrological model has great uncertainty in low-flow and high-flow regions. The reason may be related to the prior distribution of the parameters. In addition, due to the complexity of the VIC hydrological model structure, there are a large number of optional parameter groups in the model; however, only 1,000 parameter groups were analyzed in the current study.

**Calibration and verification of the VIC hydrological model.** In the process of model calibration and verification, the periods of calibration, verification and warm-up were set to 1971–1990, 1991–2000 and 1961–1970, respectively. The VIC model parameters were selected based on results described in the previous section. The detailed parameter configuration is shown in Table S1. As shown in Fig. 5a–h, the VIC model can simulate the runoff process and peak time of the PS, ZT, CT and YC stations, but the minimum and maximum values of discharge are underestimated. The NSEs of the respective PS, ZT, CT and YC stations are 0.90, 0.95, 0.96 and 0.93 during the calibration period and 0.92, 0.95, 0.95 and 0.92 during the verification period (see Table 4). The BIAS values of the respective PS, ZT, CT and YC stations are 1.41%, – 6.67%, – 2.88% and – 3.61% during the calibration period and 1.14%, – 7.88%, – 4.41% and – 5.86% during the verification period (see Table 4). The above results show that the VIC model has good simulation performance for the monthly average flow of the basin.

To further analyze the simulation performance of the VIC hydrological model with respect to the runoff process in the UYRB, we analyzed the daily runoff process in a typical wet year (1981) and a typical dry year (1994). As shown in Fig. S1 (a–d), the VIC hydrological model performs well in simulating the daily runoff process in the UYRB. The coefficient of determination ( $R^2$ ) between the observed and simulated daily runoff at the PS, ZT,



**Figure 4.** Uncertainty interval of monthly mean runoff at the 95% confidence level during the validation period. (a PS station; b ZT station; c CT station; d YC station). The figure was generated by MATLAB2019a (<https://www.mathworks.com/>).

Indices	PS	ZT	CT	YC
CR	77.5	98.3	79.2	75.3
B	3175	10,736	6201	9732
S	0.31	0.25	0.29	0.35

**Table 3.** Evaluation indices of the uncertainty interval during the validation period.

CT and YC stations reaches 0.9, 0.92, 0.91 and 0.91, respectively (Fig. S1). As shown in Fig. S2, the NSEs of the respective PS, ZT, CT and YC stations are 0.9, 0.93, 0.92 and 0.9 in the wet year (Fig. S2a, c, e, g) and 0.68, 0.85, 0.86 and 0.81 in the dry year (Fig. S2b, d, f, g). The BIAS values of the four stations are 13.52%, -0.45%, 0.32% and 0.33% in the wet year and -5.56%, -9.33%, -0.55% and -0.41% in the dry year (see Table S2). In general, the VIC hydrological model has good applicability in the UYRB, and its simulation performance in the wet year is slightly better than that in the dry year.

**Trend analysis.** The nonparametric Mann–Kendall (MK) method<sup>62,63</sup> was used to analyze the temporal trends of climatic factors, with significance evaluated at the 95% confidence level. The nonparametric MK method is considered a simple and effective way of conducting climate change analysis and has been extensively used in the analysis of hydrometeorological time series sets<sup>50,64</sup>. The MK statistical test is given as follow:

$$Z = \begin{cases} \frac{S - 1}{\sqrt{\text{Var}(S)}} & S > 0 \\ 0 & S = 0 \\ \frac{S + 1}{\sqrt{\text{Var}(S)}} & S < 0 \end{cases} \quad (16)$$

where statistic S can be calculated as:

$$S = \sum_{i=1}^{n-1} \sum_{j=i+1}^n \text{sgn}(x_j - x_i) \quad (17)$$

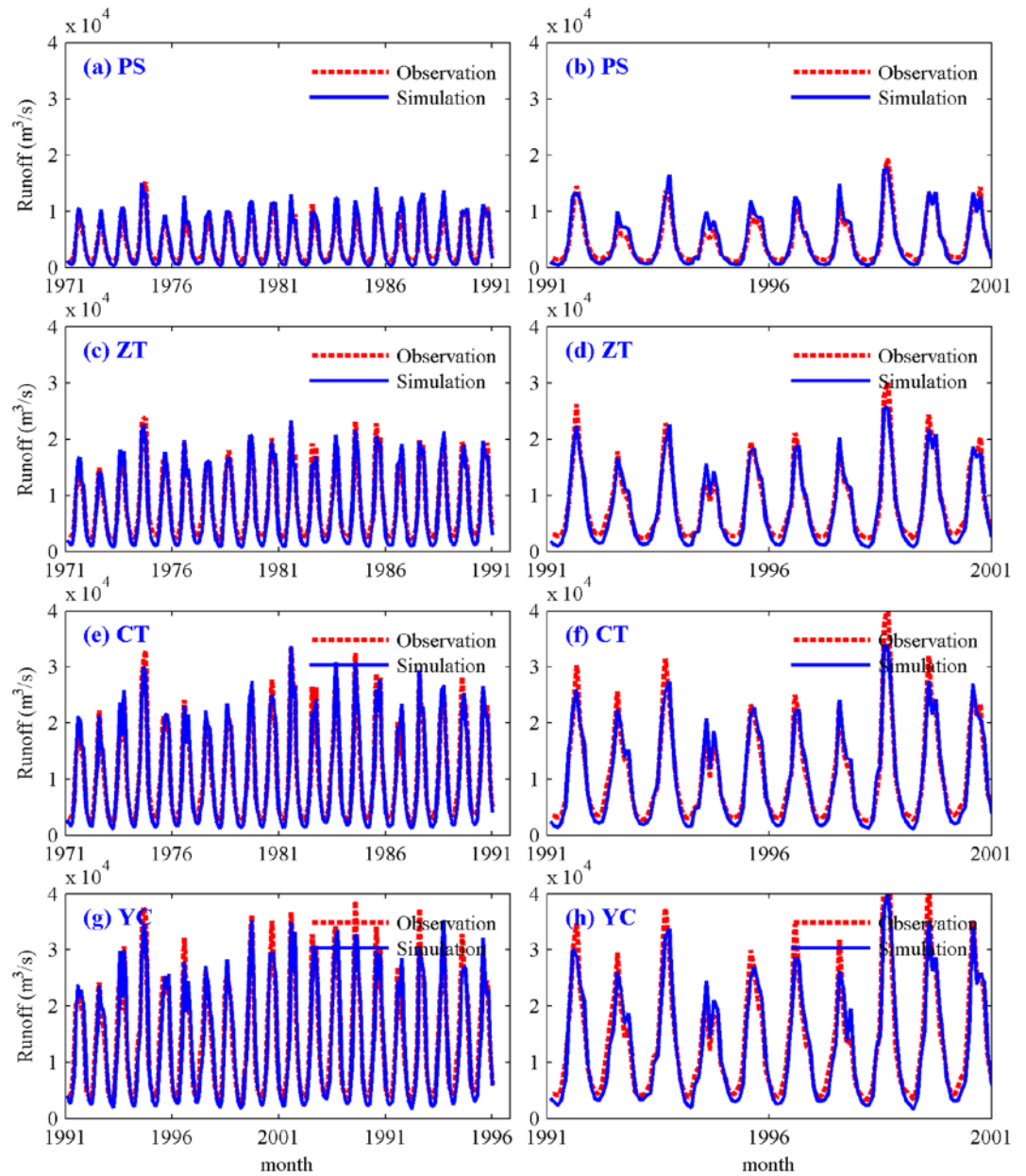


**Figure 5.** Comparisons of simulated and observed monthly mean runoff processes during calibration (a,c,e,g) and verification (b,d,f,h) periods. The figure was generated by MATLAB2019a (<https://www.mathworks.com/>).

Station	Calibration period		Verification period	
	NSE	BIAS (%)	NSE	BIAS (%)
PS	0.90	1.41	0.92	1.14
ZT	0.95	- 6.67	0.95	- 7.88
CT	0.96	- 2.88	0.95	- 4.41
YC	0.93	- 3.61	0.92	- 5.87

**Table 4.** Simulation performance of monthly mean runoff during the calibration and validation periods.



ID	Station	Name	Latitude	Longitude	ID	Station	Name	Latitude	Longitude
1	52908	Wudaoliang	35.3°	93.6°	22	56565	Yanyuan	27.4°	101.6°
2	56004	Tuotuohe	34°	92.6°	23	56571	Liangshan	27.9°	102.3°
3	56029	Yushu	32.9°	96.7°	24	56651	Lijiang	26.9°	100.2°
4	56034	Qingshuihe	33.9°	97.5°	25	56671	Huili	26.8°	102.3°
5	56144	Dege	31.8°	98.6°	26	56684	Huize	26.4°	103.2°
6	56146	Ganzi	31.6°	100°	27	56751	Dali	25.7°	100.2°
7	56167	Daofu	31°	101.2°	28	56778	Kunming	25°	102.7°
8	56172	Maerkang	31.9°	102.6°	29	57211	Ningqiang	32.7°	106.4°
9	56178	Xiaojin	31°	102.4°	30	57237	Wanyuan	32.1°	108.2°
10	56182	Songpan	32.6°	103.6°	31	57238	Zhenba	32.3°	108.1°
11	56188	Dujiangyan	31°	103.6°	32	57306	Langzhong	31.6°	106°
12	56385	Emeishan	29.5°	103.7°	33	57313	Bazhong	31.9°	106.8°
13	56386	Leshan	29.5°	103.8°	34	57348	Fengjie	31.1°	109.5°
14	56444	Deqin	28.8	98.8°	35	57355	Badong	31.1°	110.4°
15	56462	Jiulong	29°	101.6°	36	57405	Suining	30.5°	105.4°
16	56475	Yuexi	28.6°	102.6°	37	57411	Nanchong	30.8°	106.1°
17	56479	Shaojue	28.2°	103°	38	57445	Jianzhi	30.6°	109.6°
18	56485	Leibo	28.3°	103.6°	39	57461	Yichang	30.7°	111.1°
19	56492	Yibin	28.8°	104.5°	40	57502	Dazu	29.7°	105.7°
20	56543	Diqing	27.5°	100°	41	57517	Jiangjin	29.3°	106.3°
21	56548	Weixi	27.2°	99.5°	42	57608	Xuyong	28.2°	105.4°

**Table 5.** Meteorological stations used for the correction performance assessment.

where  $x_i$  and  $x_j$  are the observations at the  $i$ th and  $j$ th moments, respectively, and  $n$  is the length of the series. When  $x_i - x_j$  is greater than, equal to or less than 0,  $\text{sgn}(x_i - x_j)$  equals 1, 0, or  $-1$ , respectively.

The statistic  $Z$  can be used as a measure of a trend.  $Z > 0$  and  $Z < 0$  indicate increasing and decreasing trends, respectively. A larger  $|Z|$  value indicates a more significant trend. In this study, significance level was evaluated at the 0.05 level, which mean that  $Z > 1.96$  and  $Z < -1.96$  indicated significant increasing and decreasing trends, respectively.

Since the autocorrelation of a time series may affect the accuracy of trend analysis, the method developed by Yue and Wang<sup>65</sup> was used to eliminate the possible autocorrelation in the extreme precipitation data series for the UHRB. In addition, Sen's slope<sup>66</sup> was used to determine the degree of trend, as it can eliminate the impact of missing data or anomalies on the trend test. The slope is estimated by

$$\beta = \text{Median} \left[ \frac{(x_j - x_i)}{(j - i)} \right], \quad \forall j > i \quad (18)$$

where  $\beta$  is the estimate of the slope of the trend and  $x_i$  and  $x_j$  are the observations at the  $i$ th and  $j$ th moments, respectively.

**Applied data.** *Meteorological observation data.* The meteorological observation data used in the UYRB were extracted based on the CN05.1 data with a resolution of  $0.5^\circ$  developed by Wu and Gao<sup>67</sup>, which include 329 meteorological stations in the YRB. Forty-two sites with relatively high quality were selected for the performance evaluation of the bias correction, and the meteorological station information is shown in Table 5. The CN05.1 data contain all meteorological elements required by VIC hydrological models and have been extensively applied in simulation performance evaluation and the analysis of climate models<sup>33</sup>. The inverse distance weighted method was used to interpolate CN05.1 data into the computational grid center of the RegCM4.5 model and the VIC model.

*Climate model data.* The reference experimental and projected experimental results of CSIRO-MK3.6.0 and MPI-ESM-MR under the RCPs (4.5 and 8.5) were used as the initial and lateral boundary conditions for the study<sup>68,69</sup>. CSIRO-MK3.6.0 and MPI-ESM-MR were submitted by the Max Planck Institute of Germany and the Commonwealth Scientific and Industrial Research Organization of Australia, respectively, to the Coupled Model Intercomparison Project Phase 5 (CMIP5). The difference between the near-future period (2021–2050) and the reference period (1971–2000) under the RCPs (4.5 and 8.5) was considered to be the climate change in the UYRB.

*VIC model forcing data.* The hydrological data used for calibration and verification of the VIC hydrological model are the daily flow data of the PS, ZT, CT and YC stations from 1961 to 2000. The basic information of

Station	Longitude	Latitude
PS	104.14°	28.64°
ZT	105.85°	29.02°
CT	106.57°	29.59°
YC	111.18°	30.77°

**Table 6.** Geographic location information of hydrological stations.

ID	Function	D	$P_{95}$	MRE	RMSE	SSE	CORR
1	Gamma	0.32	23	20.59	6.87	1.66	1.00
2	Exponential	0.54	8	54.90	27.08	22.74	0.98
3	Gumbel	0.80	0	164.92	43.75	63.23	0.94
4	GP	0.51	0	-49.63	15.28	8.45	0.99
5	GEV	0.38	14	9.32	13.44	6.01	0.99
6	G-G	0.18	38	1.17	1.39	0.16	1.00
7	G-E	0.19	40	-1.26	1.35	0.18	1.00
8	G-U	0.37	13	8.10	3.17	0.38	1.00
9	G-V	0.17	39	-1.07	1.29	0.14	1.00
10	G-P	0.23	16	-0.66	2.04	0.46	1.00

**Table 7.** Statistical parameters of the fitting performance.

the hydrological station is shown in Table 6. The topography of the UYRB was defined from a digital elevation model (DEM) than can be downloaded from the website: <http://www.gscloud.cn>. The soil data were extracted from the global 5-min soil data set from the NOAA hydrological office (<http://www.fao.org/soils-portal/en/>). The vegetation cover data were obtained from the land cover classification data set with a 1 km resolution from the University of Maryland (<http://www.landcover.org/data/landcover/data.shtml>).

## Results

**Bias correction using the QM method.** *Correction performance for different distributions.* To evaluate the performance of the QM method based on the mixture distribution for precipitation correction, observed precipitation data from 42 stations with good quality in the UYRB were applied. Table 7 shows the fitting performance statistical parameters of the QM method based on different distributions, such as the statistics of the Kolmogorov–Smirnov test ( $D$ ), number of stations passing the Kolmogorov–Smirnov test at the 95% confidence level ( $P_{95}$ ), root mean square error ( $RMSE$ ), mean relative error ( $MRE$ ), sum of squares due to error ( $SSE$ ) and  $CORR$ . According to the results in Table 7, the QM method based on mixed distribution has significantly better fitting performance regarding observed precipitation than that based on a single distribution. In the statistical results of the QM method based on the single distribution, few stations passed the significance test at the 95% confidence level, indicating that the single distribution fitting the observed precipitation in the UYRB is not applicable. The fitting performance of the mixed distribution for observed precipitation in the UYRB was significantly higher than that of the single distribution, especially G-G, G-E and G-V. The statistical results in Table 7 show that among all the mixed distributions, the G-V distribution achieved the best overall performance. Therefore, the G-V distribution was selected to correct precipitation data from the RegCM4.5 output.

*Bias correction using the G-V distribution.* Figure 6 shows the Taylor diagrams of various meteorological elements in the UYRB before and after the revision from the CSIRO-MK3.6.0 and MPI-ESM-MR downscaling results (defined as R\_CS and R\_MPI, respectively) for the reference period. As shown in Fig. 6(a-c), poor performance was achieved in precipitation simulation in the UYRB from R\_CS and R\_MPI before the correction (marked in red). The spatial correlation coefficient of annual precipitation between simulated and observed precipitation was only approximately 0.1, whereas it can reach approximately 0.35 in winter, and the precipitation overestimation usually exceeded 20%. After the correction (marked in blue), the spatial correlation coefficient of annual precipitation between simulated and observed precipitation increased from 0.1 to 0.99, and the precipitation bias was reduced to approximately 10%.

As shown in Fig. 6d–l, the annual average air temperature ( $T_{2m}$ ), minimum temperature ( $T_{min}$ ), and maximum temperature ( $T_{max}$ ) were typically well simulated even before the correction (marked in red), and the spatial correlation coefficient of the air temperature between the simulated and observed values was usually approximately 0.95. The average annual and summer air temperatures had a warm bias of approximately 20% compared with an approximately 20% cold bias in winter. After the correction (marked in blue), the spatial correlation coefficient of the air temperature between the simulated and observed values increased from 0.95 to 0.99, and the bias of the air temperature was reduced from 20 to 10%.

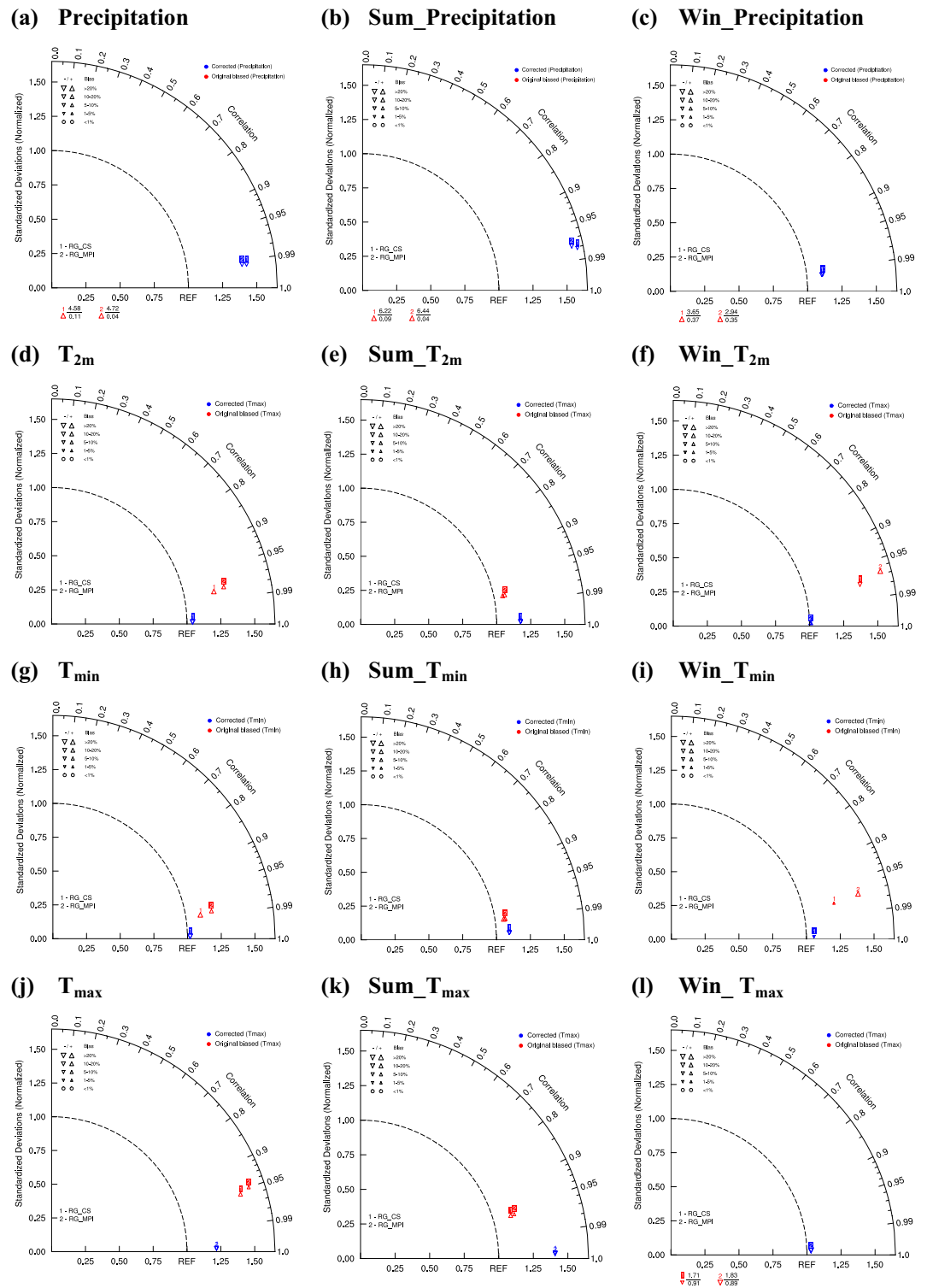


**Figure 6.** Taylor diagrams of precipitation (a–c),  $T_{2m}$  (d–f),  $T_{min}$  (g–i) and  $T_{max}$  (j–l) before and after the revision from R\_CS and R\_MPI for the reference period. (annual, left panels; summer, middle panels; winter, right panels). The figure was prepared using The NCAR Command Language version 6.5.0. (<https://doi.org/10.5065/D6WD3XH5>).

Figure 7 shows the annual cycles of precipitation,  $T_{2m}$ ,  $T_{max}$  and  $T_{min}$  before and after the revision from R\_CS and R\_MPI. As shown in Fig. 7a, the unrevised precipitation from R\_CS and R\_MPI was overestimated in the UYRB, whereas the revised precipitation was consistent with the observations. Similarly, compared with the

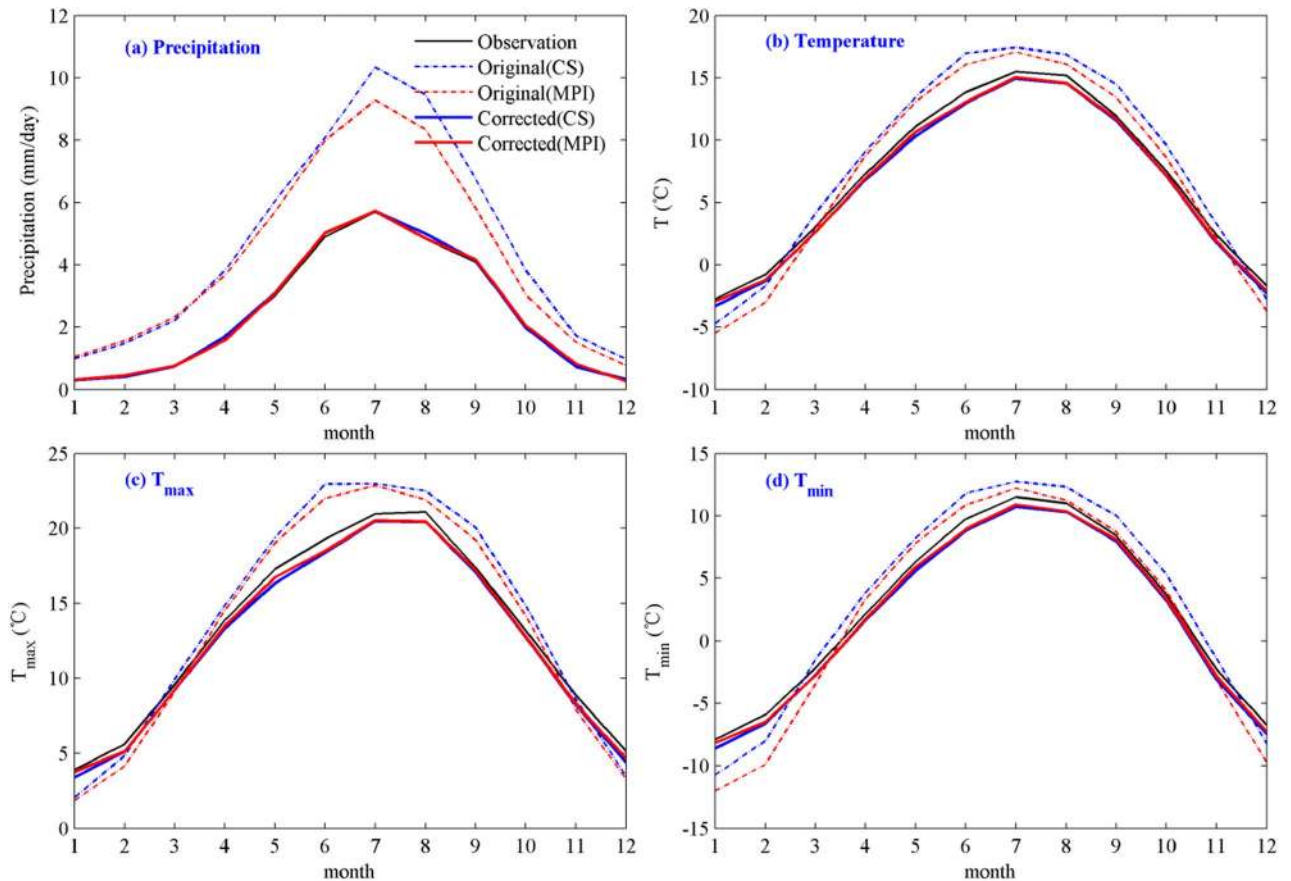


**Figure 7.** Annual cycles of precipitation (a),  $T_{2m}$  (b),  $T_{max}$  (c) and  $T_{min}$  (d) before and after the revision from R\_CS and R\_MPI. (The black line represents the observation; the blue and red dashed lines represent the result before the R\_CS and R\_MPI corrections, respectively; the blue and red lines represent the result after the R\_CS and R\_MPI corrections, respectively). The figure was generated by MATLAB2019a (<https://www.mathworks.com/>).

observations,  $T_{2m}$ ,  $T_{max}$  and  $T_{min}$  before the revision exhibited some deviation in the annual cycle, among which warm biases mainly occurred in spring, summer and autumn, while cold biases occurred in winter (Fig. 7b–d). After the correction, the warm and cold biases were greatly reduced, and the annual cycle of temperature was consistent with the observation.

To further understand the performance of the correction using the QM method, Figs. S3–S6 (a–o) show the spatial distribution of annual mean precipitation,  $T_{2m}$ ,  $T_{max}$  and  $T_{min}$  in the UYRB before and after the revision from R\_CS and R\_MPI, and the corresponding results for summer and winter are also presented. After the revision, the precipitation biases that prevailed in the mountainous areas from western Sichuan to southern Qinghai and the southeastern region of the UYRB were significantly improved, and the warm bias of the Sichuan Basin and the cold bias of the source area of the YRB were significantly improved (Fig. S3–S6). In short, the simulation performance regarding precipitation and air temperature from R\_CS and R\_MPI was greatly improved after correction using the QM method. From the next section onward, all meteorological elements referring to R\_CS and R\_MPI are corrected using the QM method.

**Near-future climate change projected by RegCM4.5.** *Near-future precipitation projected by RegCM4.5.* Figure 8 shows the changes in the multiyear average precipitation under the RCPs (4.5 and 8.5) for R\_CS (Fig. 8a,b) and R\_MPI (Fig. 8c,d) in the mid-twenty-first century (defined as 2021–2050 minus 1971–2000). The block diagram shows the interannual variation trend in multiyear average precipitation anomaly. The black dotted shows the changes that passed the significance test. In general, the multiyear average precipitation of the UYRB from R\_CS and R\_MPI during the 2021–2050 period exhibited an insignificant downward trend. Based on the spatial distribution of precipitation, there are obvious differences between the east and west of the UYRB. As shown in Fig. 8, the multiyear average precipitation in the Sichuan Basin increased significantly in the northwestern areas but decreased significantly in the southeast areas. Compared with the reference period, the multiyear average precipitation in the future will increase significantly by approximately 0.5 mm/day in the northwestern part of the basin and will decrease significantly by approximately 0.5 mm/day in the southeast of the basin.

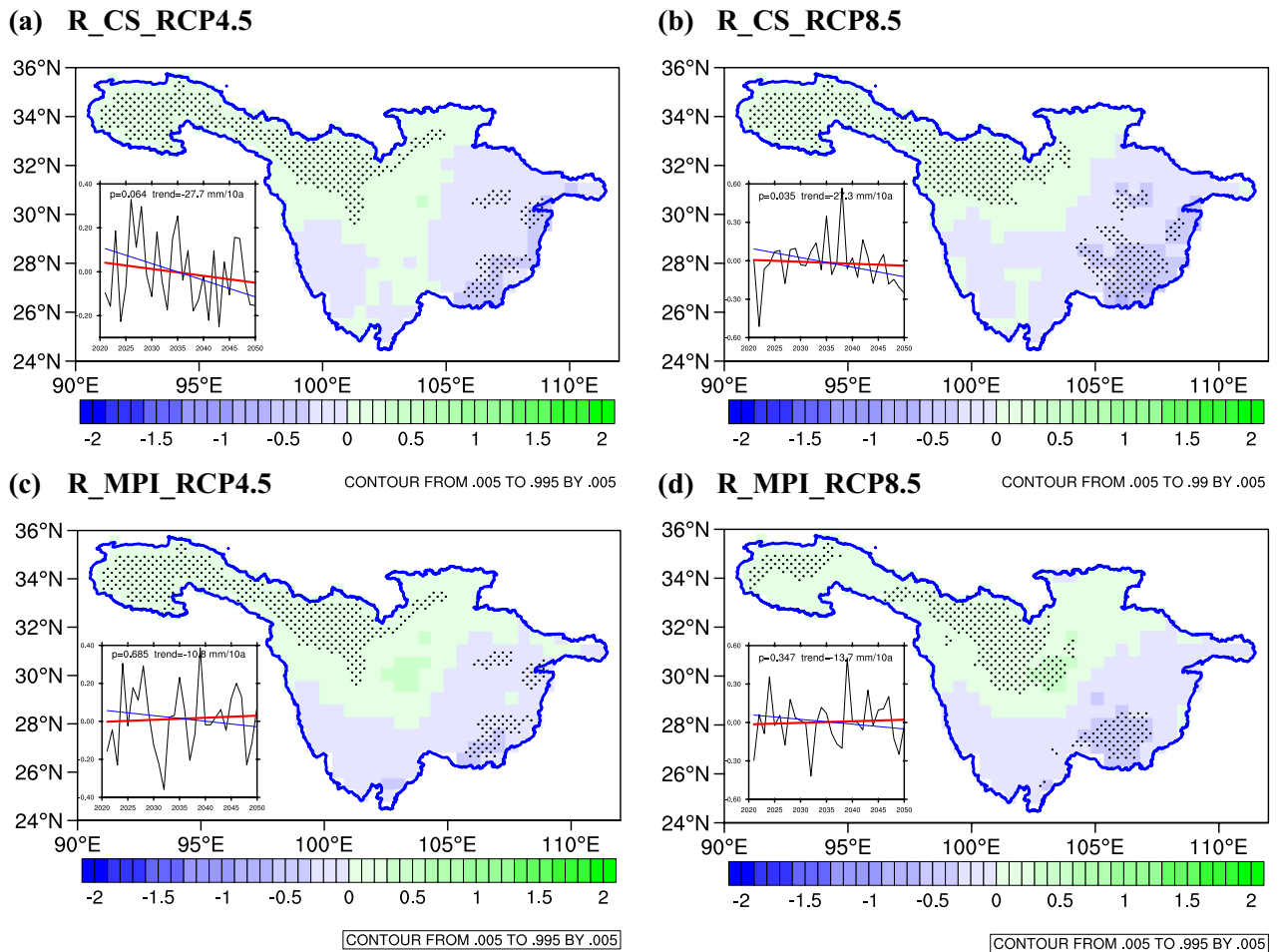


**Figure 8.** Multiyear average changes (unit: mm/day) in precipitation over the UYRB under the RCP4.5 and RCP8.5 scenarios compared to the reference period (1971–2000). The black dots denote differences that are statistically significant at a significance level of 95% based on Student’s t-test. The rectangle indicates the interannual variation trend of precipitation anomalies (unit: mm/day). The figure was prepared using The NCAR Command Language version 6.5.0. (<https://doi.org/10.5065/D6WD3XH5>).

Periods	R_CS		R_MPI		Average	
	RCP4.5	RCP8.5	RCP4.5	RCP8.5	RCP4.5	RCP8.5
2021–2030	0.025	– 0.047	0.012	0.036	0.018	– 0.006
2031–2040	0.010	0.086	– 0.014	– 0.019	– 0.002	0.033
2041–2050	– 0.048	– 0.088	0.020	0.018	– 0.014	– 0.035
Mean	– 0.004	– 0.016	0.006	0.011	0.001	– 0.002
Trend (mm/10 a)	– 27.7	– 27.3*	– 10.8	– 13.7	– 19.25	– 19.05

**Table 8.** Changes and trends of precipitation from R\_CS and R\_MPI under the RCP4.5 and RCP8.5 scenarios in different periods. \*indicates a significant value at the 0.01 level. \*\*indicates a significant value at the 0.05 level.

Table 8 shows the variation of multiyear average precipitation in different periods under the RCPs (4.5 and 8.5) compared with the reference period. Under the RCPs (4.5 and 8.5), the changes in precipitation projected by R\_CS and R\_MPI in different periods were slightly different, but precipitation in both projections generally showed a trend of first increasing and then decreasing. In R\_CS, the precipitation decrease was concentrated in 2031–2040 and was reduced by 0.048 mm/day and 0.088 mm/day under the RCP4.5 and RCP8.5, respectively. In R\_MPI, the degree of precipitation decrease was smaller than that of R\_CS, and the precipitation decrease was concentrated in 2040–2050. During this period, the precipitation decreases by 0.014 mm/day and 0.035 mm/day under the RCP4.5 and RCP8.5, respectively.

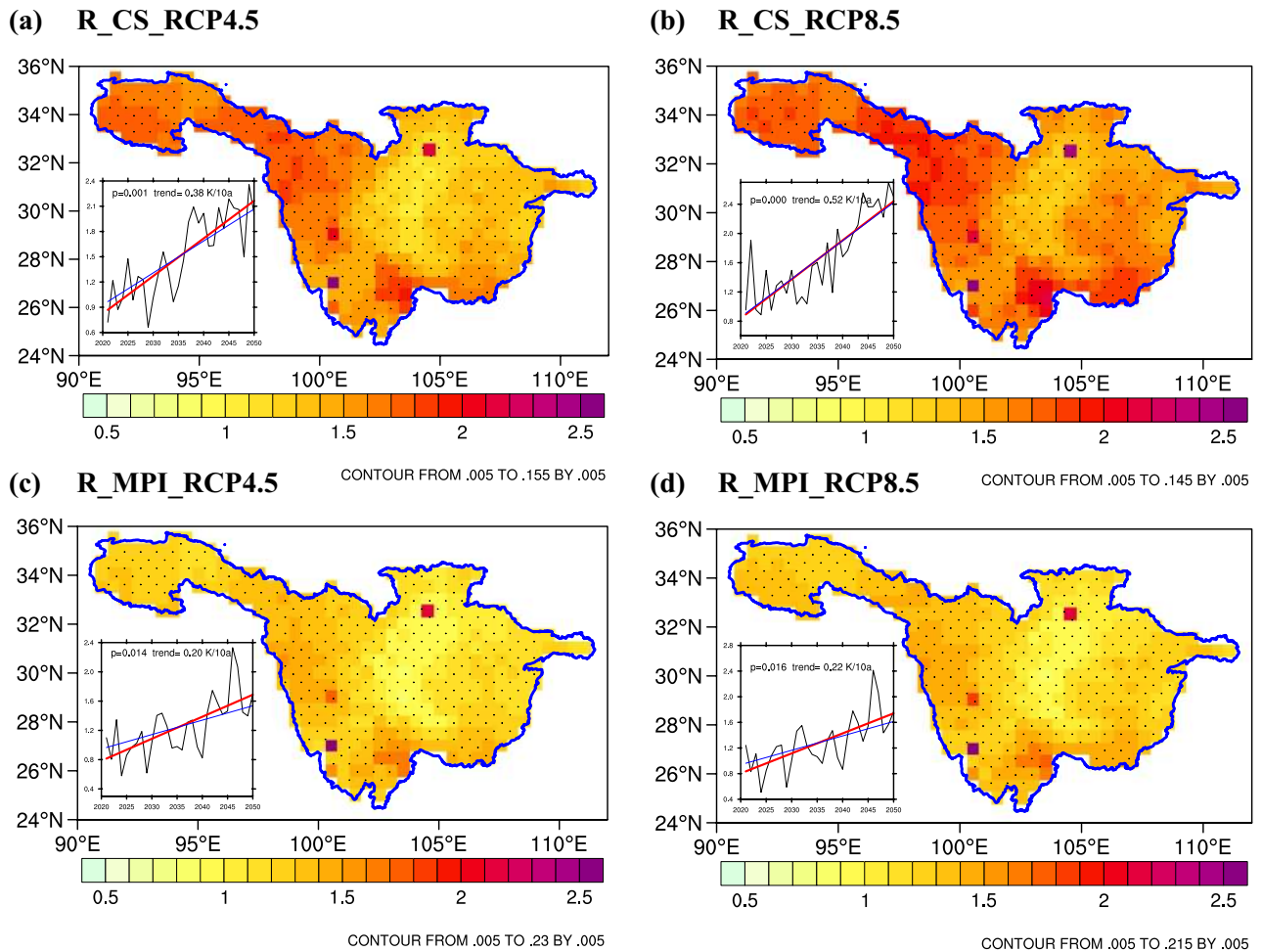


**Figure 9.** Multiyear average changes (unit: °C) in  $T_{2m}$  over the UYRB under the RCP4.5 and RCP8.5 scenarios compared to the reference period (1971–2000). The black dots denote differences that are statistically significant at a significance level of 95% based on Student’s t-test. The rectangle indicates the interannual variation trend of air temperature anomalies (unit: °C/10 a). The figure was prepared using The NCAR Command Language version 6.5.0. (<https://doi.org/10.5065/D6WD3XH5>).

Periods	R_CS		R_MPI		Average	
	RCP4.5	RCP8.5	RCP4.5	RCP8.5	RCP4.5	RCP8.5
2021–2030	1.046	1.247	0.967	0.952	1.007	1.099
2031–2040	1.567	1.446	1.141	1.208	1.354	1.327
2041–2050	1.937	2.305	1.660	1.688	1.798	1.997
Mean	1.516	1.666	1.256	1.283	1.386	1.474
Trend (°C/10 a)	0.38**	0.52**	0.20*	0.22*	0.29*	0.37*

**Table 9.** Changes and trends of  $T_{2m}$  from R\_CS and R\_MPI under the RCP4.5 and RCP8.5 scenarios in different periods. \*indicates a significant value at the 0.01 level. \*\*indicates a significant value at the 0.05 level.

*Near-future temperature projected by RegCM4.5.* Figure 9 and Figures S7–S8 show the changes in the multiyear average  $T_{2m}$  (Fig. 9a–d),  $T_{max}$  and  $T_{min}$  under the RCPs (4.5 and 8.5) for R\_CS (Fig. 9a,b, S7a,b and S8a,b) and R\_MPI (Fig. 9c,d, S7c,d and S8c,d) in the mid-twenty-first century (defined as 2021–2050 minus 1971–2000). In general, compared with the reference period, the multiyear average  $T_{2m}$  of the UYRB will increase by approximately 1–1.5 °C in the future, and the increasing trend will reach 0.29 °C/10 a and 0.37 °C/10 a under RCP4.5 and RCP8.5, respectively. In the future, the greater temperature increase will be mainly concentrated in the area from the Songpan Plateau to the east of the Qinghai-Tibet Plateau, where the  $T_{max}$  and  $T_{min}$  increases are usually above 2 °C. Table 9 and Tables S3–S4 show the variation of the multiyear average  $T_{2m}$ ,  $T_{max}$  and  $T_{min}$  in different periods under the RCPs (4.5 and 8.5) compared with the reference period. It can be seen from Table 9 that the

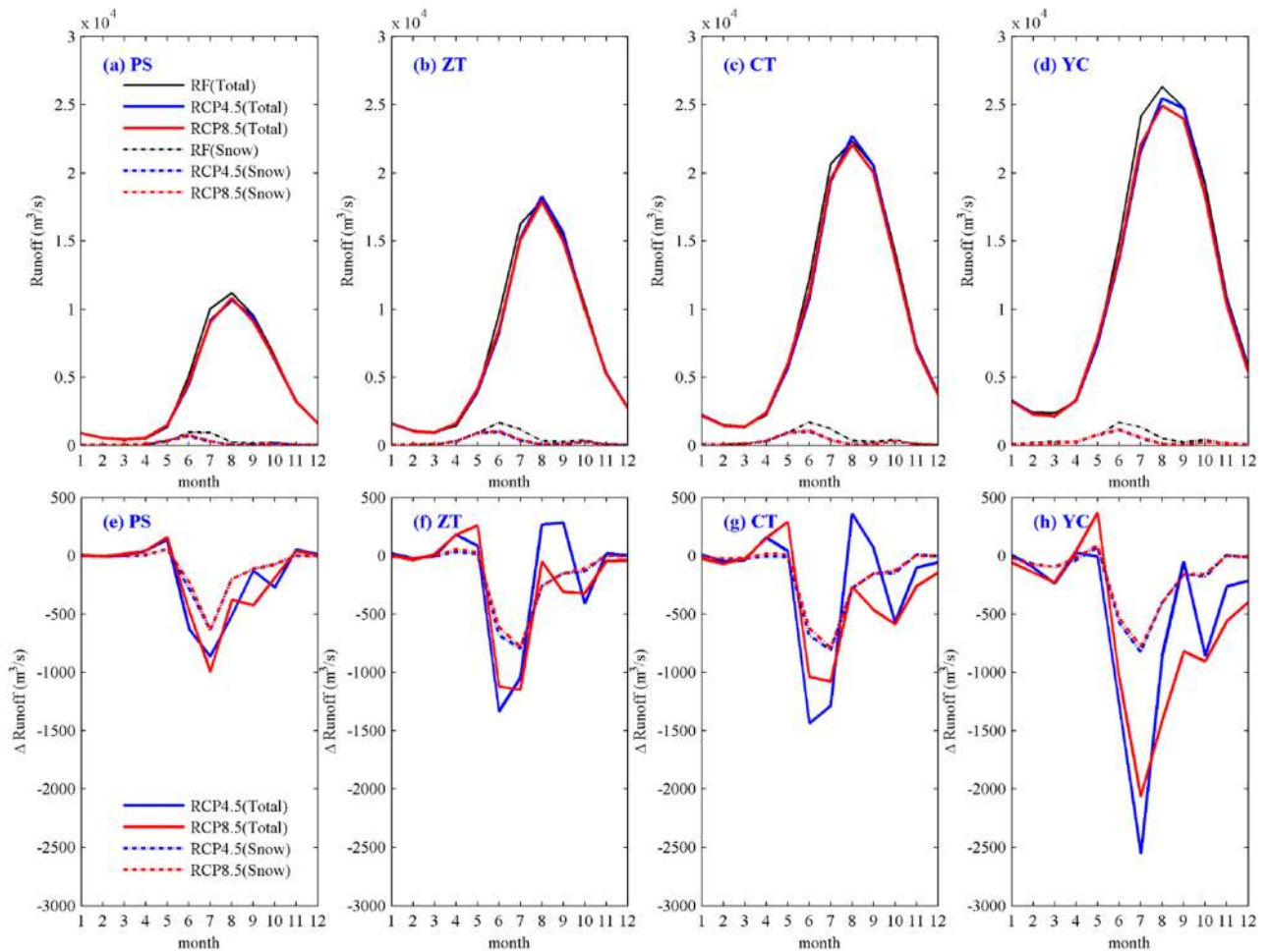


**Figure 10.** The multiyear average runoff process (a–d) of the  $R_t$  (solid line) and  $R_s$  (dashed line) for the PS, ZT, CT and YC stations under the RCP4.5 and RCP8.5 scenarios and the corresponding changes (e–h). (The black color represents the reference period; the blue and red colors represent RCP4.5 and RCP8.5, respectively). The figure was generated by MATLAB2019a (<https://www.mathworks.com/>).

$T_{2m}$  increase is approximately 1 °C during the 2021–2030 period, while by the middle of the twenty-first century, the  $T_{2m}$  increase will reach approximately 1.5–2 °C.

In the future, the spatial changes of precipitation and temperature will be quite different between the western and eastern areas of the UYRB. On the whole, the eastern part of the basin shows a warm and dry trend, while the western part of the basin shows a warm and wet trend. Precipitation has strong interdecadal variation characteristics from 2021 to 2050, with a trend of first increasing and then decreasing, but the above trends are not significant. However, the temperature from 2021 to 2050 will continue to increase significantly, and the rate of warming will accelerate significantly.

**Near-future changes in runoff.** *Seasonal variation characteristics of runoff.* To study the characteristics of runoff changes under the near-future climate change in the UYRB, the average climate fields of  $R_{CS}$  and  $R_{MPI}$  were used as forcing data of the VIC hydrological model to simulate the near-future runoff process. Figure 10a–d shows the multiyear average runoff process of the total runoff ( $R_t$ , solid line) and snowmelt runoff ( $R_s$ , dashed line) for the PS, ZT, CT and YC stations under the RCPs (4.5 and 8.5), and the corresponding changes are presented (defined as the values in 2021–2050 minus those in 1971–2000). As shown in Fig. 10, compared with those in other seasons, the summer  $R_t$  and  $R_s$  will decrease more in the near-future. As shown in Fig. 10e–g, the decrease in  $R_t$  for the PS, ZT and CT stations located in the middle and upper reaches of the UYRB is largely due to the contribution of  $R_s$ , whereas the decrease in  $R_t$  for the YC station at the outlet of the UYRB is less affected by  $R_s$  (Fig. 10 h). Table 10 shows the contribution of  $R_s$  to  $R_t$  in different seasons. In terms of the annual average, the  $R_s$  of the PS, ZT, CT and YC stations accounts for 5.9%, 6.0%, 4.8% and 4.1%, respectively, of the  $R_t$ . The  $R_s$  contributes the most to the  $R_t$  in spring, with contributions of 17.8%, 19.5% and 14.6% for the PS, ZT and CT stations, respectively, while the contribution for YC is only 9.2%. The contribution of  $R_s$  to  $R_t$  is approximately 5–8% in summer but only approximately 1–2% in autumn and winter.

Table 11 shows the multiyear average changes for the PS, ZT, CT and YC stations in different seasons under the RCPs (4.5 and 8.5) relative to the reference period. According to the results of the YC station at the outlet of the UYRB,  $R_t$  will decrease by approximately 4.4–5% in the near-future, while  $R_s$  will decrease by approximately

	PS	ZT	CT	YC
Spring	17.8	19.5	14.6	9.2
Summer	8.1	7.2	5.9	5.4
Autumn	2.2	2.2	1.7	1.4
Winter	1.5	2.0	1.8	3.0
Average	5.9	6.0	4.8	4.1

**Table 10.** Contribution of  $R_s$  to  $R_t$  in different seasons (unit: %).

		PS		ZT		CT		YC	
		$R_t$ (%)	$R_s$ (%)	$R_t$ (%)	$R_s$ (%)	$R_t$ (%)	$R_s$ (%)	$R_t$ (%)	$R_s$ (%)
RCP4.5	Spring	8.3	15.2	4.2	3.6	1.7	-2.7	-1.7	-5.0
	Summer	-7.6	-52.7	-4.8	-55.1	-4.3	-54.5	-7.2	-51.0
	Autumn	-1.8	-44.8	-0.3	-39.7	-1.4	-39.5	-2.1	-42.3
	Winter	0.4	-14.5	0.1	-24.4	-1.3	-24.4	-2.7	-26.1
	Average	-4.2	-42.1	-2.3	-38.7	-2.5	-38.9	-4.4	-38.9
RCP8.5	Spring	9.9	17.3	7.4	7.0	4.5	0.8	1.4	-2.1
	Summer	-7.0	-49.9	-5.3	-52.6	-4.3	-52.1	-6.9	-48.5
	Autumn	-3.0	-44.2	-2.2	-37.8	-3.1	-37.7	-4.2	-40.8
	Winter	0.2	-19.3	-1.4	-28.5	-3.2	-27.8	-5.2	-31.1
	Average	-4.31	-39.8	-3.0	-36.2	-3.1	-36.5	-5.0	-36.9

**Table 11.** Multiyear average changes (unit: %) of the  $R_t$  and  $R_s$  for the PS, ZT, CT and YC stations in different seasons under the RCP4.5 and RCP8.5 scenarios relative to the reference period.

36.9–38.9%. The variation in  $R_t$  in different seasons is quite different, among which  $R_t$  decreases by approximately 6.9–7.2% in summer, 2.1–4.2% in autumn and 2.7–5.2% in winter. Note that the  $R_t$  in spring shows a slight opposite change in the near-future between the RCP4.5 and RCP8.5. Under the RCP4.5 scenario, the  $R_t$  in spring decrease by approximately -1.7%, whereas the  $R_t$  in spring increases by approximately 1.4% under the RCP8.5 scenario, which is related to the increase in  $R_s$  caused by climate warming. It can be seen from the spring  $R_s$  of other stations that the degree of increase of the  $R_s$  under the RCP8.5 scenario is significantly higher than that under the RCP4.5 scenario. In addition, the  $R_s$  of the PS station will increase significantly in spring, which is due to the melting of a large amount of snow cover in the upper reaches of the UYRB in winter, indicating that runoff changes in the source area of the Yangtze River are highly sensitive to climate warming.

**Spatial variation characteristics of hydrological elements.** Figure 11 shows the spatial distribution of the multiyear average precipitation, runoff depth and evaporation in the UYRB in the reference period and the corresponding changes under the RCPs (4.5 and 8.5). As shown in Fig. 11a, in the reference period, the southeastern part of the UYRB is the main area of precipitation, with annual precipitation exceeding 1000 mm, while the total annual precipitation in the northwest of the UYRB is usually approximately 200 mm. The spatial pattern of the multiyear average runoff depth in the reference period is nearly the same as that of precipitation, but the spatial distribution of multiyear average variation in the near-future differs between the southeast and northwest regions of the UYRB (Fig. 11d). According to the results of “Near-future climate change projected by RegCM4.5”, precipitation will decrease in the southeast area of the UYRB and increase in the northwest (Fig. 11b,c). The runoff depth will increase only in the source area of the YRB and the Minjiang River Basin in the middle of the UYRB under the RCPs (4.5 and 8.5), by approximately 15–25%, decreasing by approximately 5–25% in the other regions (Fig. 11e,f). The spatial distribution of evaporation changes is largely consistent with that of precipitation in the near-future. As shown in Fig. 11h–i, the evaporation in the northwestern UYRB will increase by approximately 20–30% in the near-future and decreases by approximately 5% in the southeastern UYRB.

**Variation characteristics of extreme runoff.** Figure 12 shows the box plots of the mean annual runoff (MAR), the maximum 1-day daily runoff (MAX1D), and the 5th and 95th percentile of daily runoff ( $Q_5$  and  $Q_{95}$ ) for the PS, ZT, CT and YC stations in the reference and near-future periods. To illustrate the extreme runoff changes in the UYRB, the YC station at the outlet of the basin is addressed here. As shown in Fig. 12d,h, compared with that in the reference period, the MAR of the YC will decrease under RCPs (4.5 and 8.5), whereas the MAX1D of the YC will not change significantly in the near-future. Compared with the reference period, both the  $Q_5$  and  $Q_{95}$  of the YC will decrease slightly in the near-future. The degree of decrease in  $Q_5$  and  $Q_{95}$  under the RCP8.5 scenario is slightly greater than that under the RCP4.5 scenario, but the degree of change mostly does not exceed the sample interval of the reference period. Note that there are many outliers of MAX1D and  $Q_{95}$  in the near-future that exceed the statistical interval of the reference period, especially under the RCP8.5 scenario.



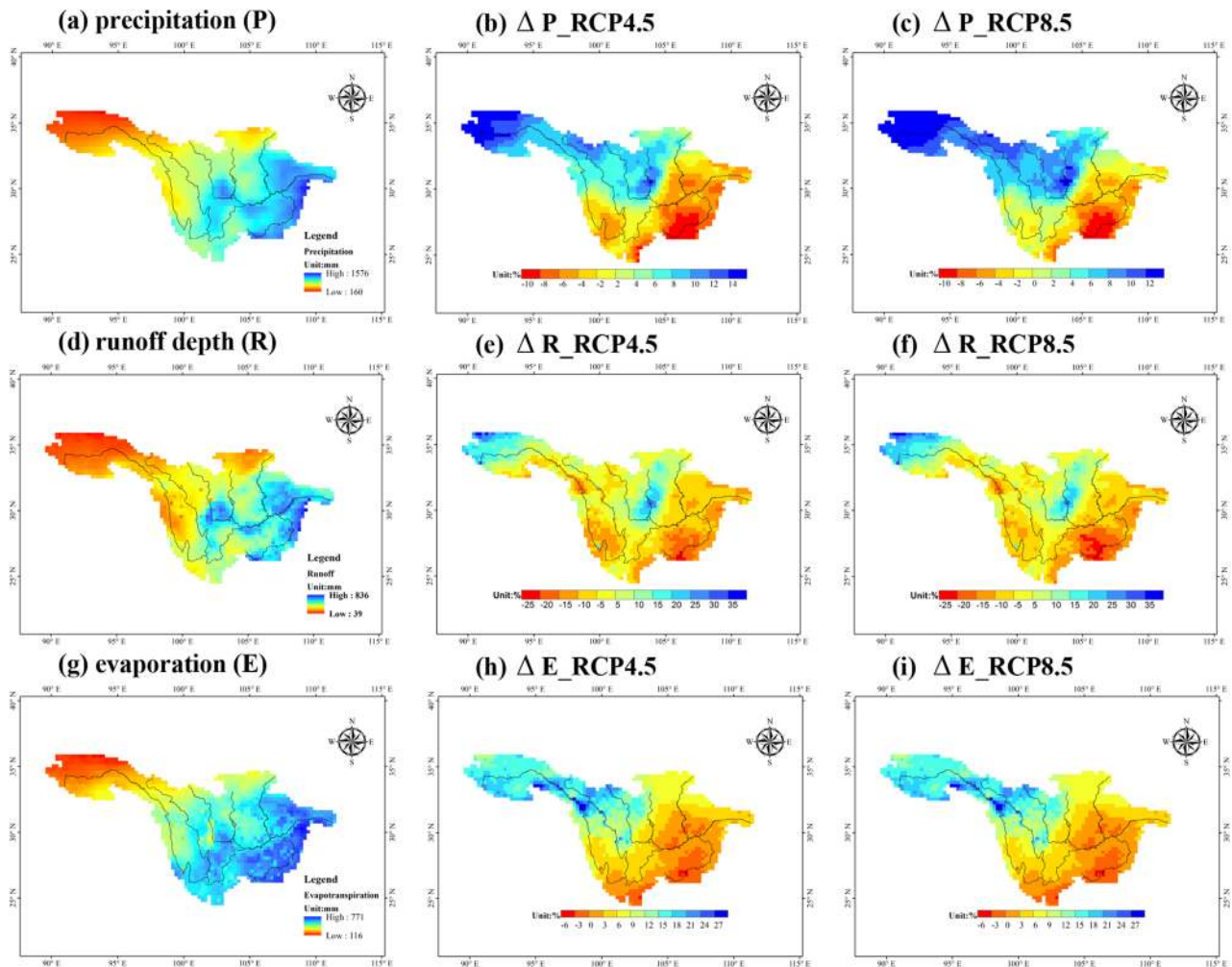


**Figure 11.** Spatial distribution of multiyear average precipitation (**a**, unit: mm), runoff depth (**d**, unit: mm) and evaporation (**g**, unit: mm) over the UYRB in the reference period and the corresponding changes (unit: %) under the RCP4.5 and RCP8.5 scenarios. The figure was generated by Arcmap 10.6 (<https://www.esri.com>).

## Discussions and conclusions

The UYRB is one of the regions in the Yangtze River Basin with frequent floods and is very sensitive to global warming. In this study, CSIRO-MK3.6.0 and MPI-ESM-MR were used to project the near-future climate change in the UYRB under RCPs (4.5 and 8.5), and meteorological elements from the dynamic downscaling results were revised using the QM method. Then, the revised climate forcing data were used to drive the hydrological model to simulate the hydrological process in the near-future over the UYRB. Finally, the spatiotemporal variation characteristics of runoff in the basin were analyzed under near-future climate changes. The main research conclusions are as follows:

According to the uncertainty analysis results, the depth of the second soil layer ( $D_2$ ) and the infiltration shape parameter ( $B$ ) are the sensitive parameters in the VIC hydrological model. The VIC hydrological model has good simulation performance for daily and monthly runoff processes in the UYRB. The  $NSE$  is usually higher than 0.9 during the calibration and verification periods, and the  $BIAS$  is within  $\pm 10\%$ , indicating that the model is appropriate for the UYRB.

According to the statistical results of  $D$ ,  $P_{95}$ ,  $MRE$ ,  $RMSE$ ,  $SSE$  and  $CORR$ , precipitation correction for the RCM results using the QM method based on a mixed distribution is better than that using the QM method based on a single distribution. The result indicates that the precipitation in the UYRB is not represented by a single precipitation pattern. In fact, the South Asian monsoon and East Asian monsoon have a strong influence on the precipitation in the YRB, so the mixed distribution can better describe the local complex precipitation pattern than the single distribution<sup>15,16</sup>. The results of Huang et al.<sup>70</sup> confirm that the EASM and its subsystem SCSSM have much greater impact on precipitation in the YRB than on that in other basins in China. Among the five mixed distributions used in the study, the Gamma-GEV has the best performance in correcting precipitation over the UYRB and can effectively correct the obvious wet biases in simulated precipitation.

According to the revised results of  $R_{CS}$  and  $R_{MPI}$ , the eastern part of the UYRB will tend to be warm and dry relative to the reference period in the near-future, whereas the western part of the basin will tend to be warm and wet. The precipitation will generally decrease at a rate of 19.05–19.25 mm/10 a, but the trend is

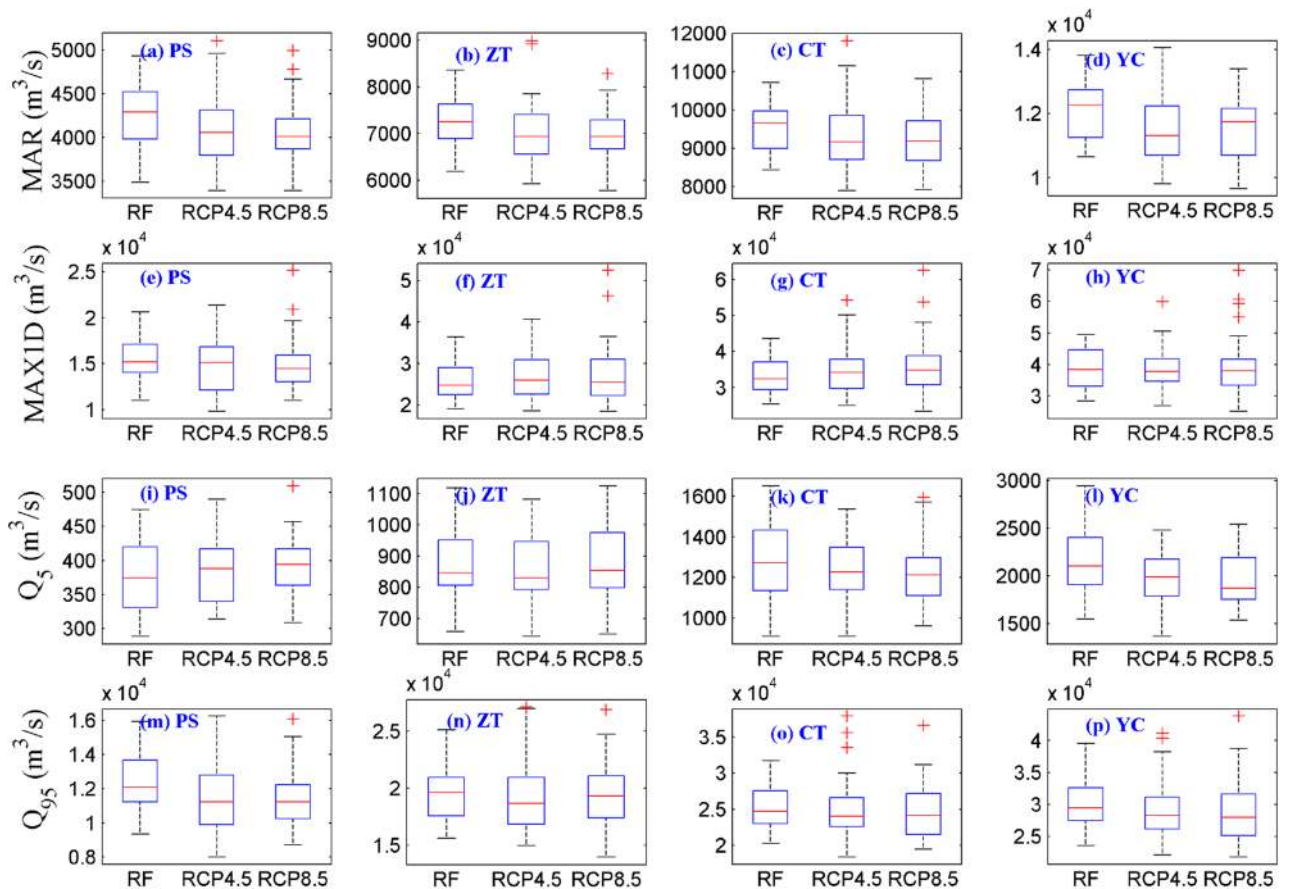


**Figure 12.** Box plots of the MAR (a–d), MAX1D (e–h), Q<sub>5</sub> (i–l) and Q<sub>95</sub> (m–p) for the PS, ZT, CT and YC stations for the reference period (RF) and future period (RCP4.5 and RCP8.5). The figure was generated by MATLAB2019a (<https://www.mathworks.com/>).

not obvious. The  $T_{2m}$  will increase significantly at a rate of 0.38–0.52 °C/10 a, and the temperature will rise by approximately 1.5 °C in the mid-twenty-first century. Huang et al.<sup>70</sup> showed that the summer precipitation in the UYRB is predicted to decrease significantly in the mid-21st century, which is consistent with the results of Cao et al., Deng et al. and Wang et al.<sup>22,30,71</sup>. Moreover, as the temperature rises, the difference in precipitation between the northwest and southeast of the basin will increase, and the risk of flood disaster caused by high-intensity precipitation in the western and central regions may increase<sup>70</sup>.

The contribution of snowmelt runoff to the annual runoff of the UYRB is only approximately 4%, and the contribution can reach approximately 9.2% in the spring. Affected by climate warming, snowmelt runoff will decrease by approximately 36–39% in the near-future, while annual runoff will decrease by approximately 4.1–5%, and extreme runoff will slightly decrease. Regarding the spatial changes in runoff depth, the areas of decreased runoff are concentrated in the southeast of the basin. The decrease in precipitation is the direct factor leading to the decrease in runoff depth in the southeast of the basin, while the decrease in runoff depth in the northwest is mainly affected by the increase in evaporation. These findings are consistent with previous studies on the impacts of climate change in the UYRB<sup>22,30,72,73</sup>. In addition, due to climate warming, more rainfall than snowfall may increase the risk of summer droughts or spring floods in the snow-covered basin, and this risk will increase as the rate of temperature rise increases<sup>30,74,75</sup>. The temperature increase in winter and spring may cause the melting of glaciers and snow at the source of the Yangtze River, where most of the glacier surface is located, and lead to a large flow increase in April<sup>30</sup>. From May to September, the water flow decreases, which may exacerbate the crisis of water shortage in the UYRB during the flood season.

However, the findings of this study are not completely consistent with some of the findings of Gu et al.<sup>29</sup> and Su et al.<sup>26</sup> Due to study differences in source data, bias correction methods, global climate models, hydrological model structure, model parameterization, reference period, comparison period, and emission scenarios, which may introduce great uncertainty in the assessment of the impact of future climate change, inconsistent results among studies may occur<sup>76</sup>. For example, Gu et al.<sup>29</sup> used the gamma distribution to revise the precipitation from the RegCM4; however, the present study revealed that a single distribution (such as the gamma distribution) was not the best choice. Compared with the mixed distribution, a single distribution will yield a large amount of wet bias in the revised precipitation, resulting in excessive precipitation, as confirmed by Shin et al.<sup>45</sup> Some studies have indicated that the uncertainty generated by the use of corrected forcing data in hydrological response studies may be of the same order of magnitude as that in the GCMs and hydrological models<sup>77,78</sup>. Previous studies have confirmed that the main source of uncertainty in future runoff forecasts in the UYRB is related to the choice

of climate forcing (GCMs and RCPs) and that hydrological models play only a secondary role<sup>26,79</sup>. However, in most previous studies, empirical manual trial calculation has been adopted to obtain the hydrological model parameters<sup>22,29</sup>, whereas in this study, the GLUE was adopted to select the optimal parameter group from a large number of sample parameters.

In this study, R\_CS and R\_MPI were used in the regional hydrological and climate projection of the UYRB, which was helpful to estimate future climate-related risks. However, it is still necessary to combine the results of more RCMs or GCMs to objectively project the climate change characteristics of the UYRB. In addition, the spatial and temporal variability of runoff may be influenced by various anthropogenic activities (e.g., irrigation, land-use change, reservoir operation), which were not considered in this study. This study aimed to provide overall and regional trends of the UYRB under a specific model, scenario, and method, rather than make accurate projections for a specific location.

Received: 4 January 2021; Accepted: 8 April 2021

Published online: 06 May 2021

## References

- Guan, X. D., Huang, J. P. & Rui, X. Changes in aridity in response to the global warming Hiatus. *J. Meteorol. Res.* **31**, 119–127 (2017).
- Zhang, Y. T., Guan, X. D., Yu, H. P., Xie, Y. K. & Jin, H. C. Contributions of radiative factors to enhanced dryland warming over East Asia. *J. Geophys. Res. Atmos.* **122**, 7723–7736 (2017).
- Song, S. K. & Bai, J. Increasing winter precipitation over arid central Asia under global warming. *Atmosphere (Basel)*. **7**, 139 (2016).
- Pfahler, J., Betts, A. K., Rizzo, D. M., Beckage, B. & Bomblied, A. Characterization of increased persistence and intensity of precipitation in the Northeastern United States. *Geophys. Res. Lett.* **42**, 1888–1893 (2015).
- Dore, M. H. I. Climate change and changes in global precipitation patterns: What do we know?. *Environ. Int.* **31**, 1167–1181 (2005).
- Pfahler, S., O Gorman, P. A. & Fischer, E. M. Understanding the regional pattern of projected future changes in extreme precipitation. *Nat. Clim. Change* **7**, 423–427 (2017).
- Tomassini, L. & Jacob, D. Spatial analysis of trends in extreme precipitation events in high-resolution climate model results and observations for Germany. *J. Geophys. Res. Atmos.* **114**, 1192 (2009).
- Coscarelli, R. & Caloiero, T. Analysis of daily and monthly rainfall concentration in southern Italy (Calabria region). *J. Hydrol.* **416–417**, 145–156 (2012).
- Caloiero, T. Analysis of daily rainfall concentration in New Zealand. *Nat. Hazards*. **72**, 389–404 (2014).
- Liu, Y. B. *et al.* Recent trends in vegetation greenness in China significantly altered annual evapotranspiration and water yield. *Environ. Res. Lett.* **11**, 94010 (2016).
- Wang, R. H. & Li, C. Spatiotemporal analysis of precipitation trends during 1961–2010 in Hubei Province, Central China. *Theor. Appl. Climatol.* **124**, 385–399 (2016).
- Yeşilirmak, E. & Atatanır, L. Spatiotemporal variability of precipitation concentration in western Turkey. *Nat. Haz.* **81**, 687–704 (2016).
- Kunkel, K. E., Pielke, R. A. J. & Changnon, S. A. Temporal fluctuations in weather and climate extremes that cause economic and human health impacts: A review. *B. Am. Meteorol. Soc.* **80**, 1077–1098 (1999).
- Easterling, D. R. *et al.* Climate extremes: Observations, modeling, and impacts. *Science* **289**, 2068–2074 (2000).
- Huang, S. S. & Yu, Z. H. On the structure of the sub-tropical highs and some associated aspects of the general circulation of atmosphere. *Acta Meteorol. Sin.* 339–359 (1962) (in Chinese).
- Tao, S. Y. & Wei, J. Correlation between monsoon surge and heavy rainfall causing flash-flood in southern China in summer. *Meteorol. Mon.* **33**, 10–18 (2007) (in Chinese).
- Sutcliffe, J. V. The use of historical records in flood frequency analysis. *J. Hydrol.* **96**, 159–171 (1987).
- Yu, Z. B., Gu, H. H., Wang, J. G., Xia, J. & Lu, B. H. Effect of projected climate change on the hydrological regime of the Yangtze River Basin, China. *Stoch. Environ. Res. Risk A.* **32**, 1–16 (2018).
- Birkinshaw, S. J. *et al.* Climate change impacts on Yangtze river discharge at the three Gorges Dam. *Hydrol. Earth Syst. Sci.* **21**, 1911–1927 (2017).
- Chen, J., Gao, C., Zeng, X., Xiong, M., Wang, Y., Jing, C., Krysanova, V., Huang, J., Zhao, N. & Su, B. Assessing changes of river discharge under global warming of 1.5 °C and 2 °C in the upper reaches of the Yangtze River Basin: Approach by using multiple-Gcms and hydrological models. *Quatern. Int.* **453**, 63–73 (2017).
- Sun, J. L., Lei, X. H., Tian, Y., Liao, W. H. & Wang, Y. H. Hydrological impacts of climate change in the upper reaches of the Yangtze River Basin. *Quatern. Int.* **304**, 62–74 (2013).
- Wang, Y. Q. *et al.* Projected effects of climate change on future hydrological regimes in the Upper Yangtze River Basin, China. *Adv. Meteorol.* **2019**, 1545746 (2019).
- Wen, S. *et al.* Comprehensive evaluation of hydrological models for climate change impact assessment in the Upper Yangtze River Basin, China. *Clim. Change*. **163**, 1207–1226 (2020).
- Xu, H., Taylor, R. G. & Xu, Y. Quantifying uncertainty in the impacts of climate change on river discharge in sub-catchments of the Yangtze and Yellow River Basins, China. *Hydrol. Earth Syst. Sci.* **15**, 333–344 (2011).
- Sun, F. Y., Mejia, A., Zeng, P. & Che, Y. Projecting meteorological, hydrological and agricultural droughts for the Yangtze River Basin. *Sci. Total Environ.* **696**, 134076 (2019).
- Su, B. D., Huang, J. L., Zeng, X. F., Gao, C. & Jiang, T. Impacts of climate change on streamflow in the Upper Yangtze River Basin. *Clim. Change* **141**, 533–546 (2017).
- Gu, H. H., Yu, Z. B., Yang, C. G. & Ju, Q. Projected changes in hydrological extremes in the Yangtze River Basin with an ensemble of regional climate simulations. *Water* **10**, 1279 (2018).
- Lu, W. J. *et al.* Hydrological projections of future climate change over the source region of Yellow River and Yangtze River in the Tibetan Plateau: A comprehensive assessment by coupling Regcm4 and Vic model. *Hydrol. Process.* **32**, 2096–2117 (2018).
- Gu, H. H. *et al.* Impact of climate change on hydrological extremes in the Yangtze River Basin, China. *Stoch. Environ. Res. Risk A.* **29**, 693–707 (2015).
- Cao, L. J., Zhang, Y. & Shi, Y. Climate change effect on hydrological processes over the Yangtze River Basin. *Quatern. Int.* **244**, 202–210 (2011).
- Gao, X. J., Zhao, Z. C., Ding, Y. H., Huang, R. H. & Giorgi, F. Climate change due to greenhouse effects in China as simulated by a regional climate model. *Acta Meteorol. Sin.* **18**, 417–427 (2003).
- Giorgi, F. *et al.* Regcm4: Model description and preliminary tests over multiple cordex domains. *Clim. Res.* **52**, 7–29 (2012).
- Gao, X. J. *et al.* Performance of Regcm4 over major river basins in China. *Adv. Atmos. Sci.* **34**, 441–455 (2017).

34. Oh, S. G., Park, J. H., Lee, S. H. & Suh, M. S. Assessment of the Regcm4 over East Asia and future precipitation change adapted to the Rcp scenarios. *J. Geophys. Res. Atmos.* **119**, 2913–2927 (2014).
35. Giorgi, F., Jones, C. & Asrar, G. R. Addressing climate information needs at the regional level: The Cordex framework. *World Meteorol. Organ. Bull.* **58**, 175–183 (2009).
36. Kiehl, T., Hack, J., Bonan, B., Boville, A. & Briegleb, P. Description of the Ncar community climate model (Ccm3). In *NCAR Technical Note NCAR/TN-420+STR*. (National Center for Atmospheric Research, 1996).
37. Emanuel, K. A. & Ivkoviorthman, M. Development and evaluation of a convection scheme for use in climate models. *J. Atmos. Sci.* **56**, 1766–1782 (1999).
38. Holtslag, A. A. M., De Bruijn, E. I. F. & Pan, H. A high resolution air mass transformation model for short-range weather forecasting. *Mon. Weather Rev.* **118**, 1561–1575 (1990).
39. Zeng, X. B., Zhao, M. & Dickinson, R. E. Intercomparison of bulk aerodynamic algorithms for the computation of sea surface fluxes using Toga Coare and Tao Data. *J. Clim.* **11**, 2628–2644 (1998).
40. Lettenmaier, D. P., Wood, A. W., Palmer, R. N., Wood, E. F. & Stakhiv, E. Z. Water resources implications of global warming: A U.S. regional perspective. *Clim. Change.* **43**, 537–579 (1999).
41. Alexandrov, V. A. & Hoogenboom, G. The impact of climate variability and change on crop yield in Bulgaria. *Agric. For. Meteorol.* **104**, 315–327 (2000).
42. Kilsby, C. G., Cowpertwait, P. S. P., O’Connell, P. E. & Jones, P. D. Predicting rainfall statistics in England and Wales using atmospheric circulation variables. *Int. J. Climatol.* **18**, 523–539 (1998).
43. Mehrotra, R. & Sharma, A. Conditional resampling of hydrologic time series using multiple predictor variables: A K-nearest neighbour approach. *Adv. Water Resour.* **29**, 987–999 (2006).
44. Leander, R. & Buishand, T. A. Resampling of regional climate model output for the simulation of extreme river flows. *J. Hydrol.* **332**, 487–496 (2007).
45. Shin, J., Lee, T., Park, T. & Kim, S. Bias correction of Rcm outputs using mixture distributions under multiple extreme weather influences. *Theor. Appl. Climatol.* **137**, 201–216 (2019).
46. Gudmundsson, L., Bremnes, J. B., Haugen, J. E. & Engen-Skaugen, T. Technical Note: Downscaling Rcm precipitation to the station scale using statistical transformations – A comparison of methods. *Hydrol. Earth Syst. Sci.* **16**, 3383–3390 (2012).
47. Themeßl, M. J., Gobiet, A. & Leuprecht, A. Empirical-statistical downscaling and error correction of daily precipitation from regional climate models. *Int. J. Climatol.* **31**, 1530–1544 (2011).
48. Gabda, D., Tawn, J. & Brown, S. A step towards efficient inference for trends in Uk extreme temperatures through distributional linkage between observations and climate model data. *Nat. Hazards.* **98**, 1135–1154 (2019).
49. Yang, T. *et al.* Regional frequency analysis and spatio-temporal pattern characterization of rainfall extremes in the Pearl River Basin, China. *J. Hydrol.* **380**, 386–405 (2010).
50. Chen, Y. D. *et al.* Precipitation extremes in the Yangtze River Basin, China: Regional frequency and spatial-temporal patterns. *Theor. Appl. Climatol.* **116**, 447–461 (2014).
51. Liang, L., Zhao, L. N., Gong, Y. F., Tian, F. Y. & Wang, Z. Probability Distribution of summer daily precipitation in the Huaihe Basin of China based on gamma distribution. *Acta Meteorol. Sin.* **26**, 72–84 (2012).
52. Liang, X. & Xie, Z. H. A new surface runoff parameterization with subgrid-scale soil heterogeneity for land surface models. *Adv. Water Resour.* **24**, 1173–1193 (2001).
53. Xu, L., Wood, E. F. & Lettenmaier, D. P. Surface soil moisture parameterization of the Vic-2L model: Evaluation and modification. *Global Planet. Change.* **13**, 195–206 (1996).
54. Shadkam, S., Ludwig, F., Vliet, M. T. H. V., Pastor, A. & Kabat, P. Preserving the world second largest hypersaline lake under future irrigation and climate change. *Sci. Total Environ.* **559**, 317–325 (2016).
55. Wang, G. Q. *et al.* Assessing water resources in China using precis projections and a Vic model. *Hydrol. Earth Syst. Sci. Discuss.* **16**, 231–240 (2012).
56. Vliet, M. T. H. V., Yearsley, J. R., Franssen, W. H. P. & Ludwig, F. Coupled daily streamflow and water temperature modelling in large river basins. *Hydrol. Earth Syst. Sc.* **16**, 4303–4321 (2012).
57. Sheffield, J. & Wood, E. F. Characteristics of global and regional drought, 1950–2000: Analysis of soil moisture data from off-line simulation of the terrestrial hydrologic cycle. *J. Geophys. Res. Atmos.* **112**, 259–262 (2007).
58. Su, F., Adam, J. C., Bowling, L. C. & Lettenmaier, D. P. Streamflow simulations of the terrestrial arctic domain. *J. Geophys. Res. Atmos.* **110**, D8112 (2005).
59. Maurer, E. P., Wood, A. W., Adam, J. C., Lettenmaier, D. P. & Nijssen, B. A long-term hydrologically based dataset of land surface fluxes and states for the conterminous United States. *J. Clim.* **15**, 3237–3251 (2002).
60. Beven, K. & Binley, A. The future of distributed models: Model calibration and uncertainty prediction. *Hydrol. Process.* **6**, 279–298 (1992).
61. Xiong, L. H., Wan, M., Wei, X. J. & O’Connor, K. M. Indices for assessing the prediction bounds of hydrological models and application by generalised likelihood uncertainty estimation. *Hydrol. Sci. J.* **54**, 852–871 (2009).
62. Kendall, M. *Rank Correlation Methods* (Griffin, 1975).
63. Mann, H. B. Nonparametric tests against trend. *Econometrica* **13**, 245–259 (1945).
64. Alexander, L. V. *et al.* Global observed changes in daily climate extremes of temperature and precipitation. *J. Geophys. Res. Atmos.* **111**, D5109 (2006).
65. Yue, S. & Wang, C. Y. Applicability of prewhitening to eliminate the influence of serial correlation on the Mann-Kendall test. *Water Resour. Res.* **38**, 1–4 (2002).
66. Sen, P. K. Estimates of the regression coefficient based on Kendall’s Tau. *J. Am. Stat. Assoc.* **63**, 1379–1389 (1968).
67. Wu, J. & Gao, X. J. A gridded daily observation dataset over China region and comparison with the other datasets. *Chin. J. Geophys.* **56**, 1102–1111 (2013) (in Chinese).
68. Rotstayn, L. D. *et al.* Aerosol- and greenhouse gas-induced changes in summer rainfall and circulation in the Australasian region: A study using single-forcing climate simulations. *Atmos. Chem. Phys.* **12**, 6377–6404 (2012).
69. Marsland, S. J., Haak, H., Jungclaus, J. H., Latif, M. & Röske, F. The Max-Planck-Institute global ocean/sea ice model with orthogonal curvilinear coordinates. *Ocean Model* **5**, 91–127 (2003).
70. Huang, Y. *et al.* Changes in seasonal and diurnal precipitation types during summer over the upper reaches of the Yangtze River Basin in the middle twenty-first century (2020–2050) as projected by Regcm4 forced by two Cmp5 global climate models. *Theor. Appl. Climatol.* **142**, 1055–1070 (2020).
71. Deng, H. Q., Luo, Y., Yao, Y. & Liu, C. Spring and summer precipitation changes from 1880 to 2011 and the future projections from Cmp5 models in the Yangtze River Basin, China. *Quatern. Int.* **304**, 95–106 (2013).
72. Wang, Y. H. *et al.* Water resource spatiotemporal pattern evaluation of the upstream Yangtze river corresponding to climate changes. *Quatern. Int.* **380–381**, 187–196 (2015).
73. Zeng, X. F., Kundzewicz, Z. W., Zhou, J. Z. & Su, B. D. Discharge projection in the Yangtze River Basin under different emission scenarios based on the artificial neural networks. *Quatern. Int.* **282**, 113–121 (2012).
74. Callaghan, T. V. *et al.* Multiple effects of changes in arctic snow cover. *Ambio* **40**, 32–45 (2011).
75. Trenberth, K. E. Changes in precipitation with climate change. *Clim. Res.* **47**, 123–138 (2011).

76. Knutti, R. & Sedláček, J. Robustness and uncertainties in the new Cmp5 climate model projections. *Nat. Clim. Change*. **3**, 369–373 (2013).
77. Ehret, U., Zehe, E., Wulfmeyer, V., Warrach-Sagi, K. & Liebert, J. Hess opinions “should we apply bias correction to global and regional climate model data?”. *Hydrol. Earth Syst. Sci.* **16**, 3391–3404 (2012).
78. Hagemann, S. *et al.* Impact of a statistical bias correction on the projected hydrological changes obtained from three Gcms and two hydrology models. *J. Hydrometeorol.* **12**, 556–578 (2011).
79. Hagemann, S. *et al.* Climate change impact on available water resources obtained using multiple global climate and hydrology models. *Earth Syst. Dynam.* **4**, 129–144 (2013).

## Acknowledgements

The authors greatly appreciate the data availability and service provided by the RegCM, ERA-Interim science team. The authors also appreciate the support of Dr. Ying Shi (Researcher, China Meteorological Administration, China) for providing the regional climate models and observational data sets used in this study. High-performance computing resources were provided by the national super-computer in Tianjin, China. This study was jointly funded by the National Key Research and Development Program (No. 2017YFC0404701, No.2018YFC1508200), the National Natural Science Foundation of China (No. 51779271 and No. 51909275), and the Innovation Project of Guangxi Graduate Education (YCBZ2018023). The ERA-interim data used in this study were obtained from <http://clima-dods.ictp.it/Data>. The observation data used in this study were obtained from <http://data.cma.cn/data>.

## Author contributions

Y.H.: Conceptualization, Methodology, Formal analysis, Investigation, Data curation, Writing-original draft, Writing-review & editing. W.X.: Validation, Writing-review & editing, Funding acquisition. B.H.: Conceptualization, Writing review & editing. Y.Z.: Methodology, Investigation. G.H.: Validation, Methodology. L.Y.: Methodology. H.C.: Writing-review & editing.

## Competing interests

The authors declare no competing interests.

## Additional information

**Supplementary Information** The online version contains supplementary material available at <https://doi.org/10.1038/s41598-021-88135-5>.

**Correspondence** and requests for materials should be addressed to Y.H.

**Reprints and permissions information** is available at [www.nature.com/reprints](http://www.nature.com/reprints).

**Publisher's note** Springer Nature remains neutral with regard to jurisdictional claims in published maps and institutional affiliations.



**Open Access** This article is licensed under a Creative Commons Attribution 4.0 International License, which permits use, sharing, adaptation, distribution and reproduction in any medium or format, as long as you give appropriate credit to the original author(s) and the source, provide a link to the Creative Commons licence, and indicate if changes were made. The images or other third party material in this article are included in the article's Creative Commons licence, unless indicated otherwise in a credit line to the material. If material is not included in the article's Creative Commons licence and your intended use is not permitted by statutory regulation or exceeds the permitted use, you will need to obtain permission directly from the copyright holder. To view a copy of this licence, visit <http://creativecommons.org/licenses/by/4.0/>.

© The Author(s) 2021